



Department of Geography

Faculty of Sciences

Université de Liège

Master's thesis in Geographic Sciences:  
Geomatics, professional focus in geodata expert

# Assessing building damage after a seismic event using unsupervised change detection with Sentinel-1 imagery

**Presented by Augustin MARTINET**

Defence date: January 2025

---

Supervisor: Prof. Francois Jonard

Jury: Prof. René Warnant

Prof. Roland Billen

2024-2025

*I would like to sincerely thank Prof. François Jonard for following this project as my supervisor and for providing constructive feedback.*

*I am also deeply grateful to Prof. Nascetti, who suggested this topic in alignment with my interests and aspirations, and for guiding the most part of my approach. I learned a lot.*

*Finally, a special thank you to my partner for her unwavering support and encouragement throughout this journey.*

---

## Abstract

Earthquake impact assessment is crucial for providing timely information for disaster relief and post-disaster reconstruction. The role of remote sensing at each stage of the risk management system has been growing with the amount, timeliness, and availability of satellite imagery in recent years. In particular, radar imagery time series offer many advantages that unsupervised change detection can employ for building damage assessment.

This work explores an unsupervised and multitemporal change detection method using Sentinel-1 imagery to assess building damage after the 2023 seismic event in Turkey.

First, a dataset of destroyed buildings was prepared from the review of Copernicus Emergency Management System (CEMS) rapid mapping products through visual analysis of optical images before and after event. A time series of the mean backscatter intensity from return signal within the footprint of each destroyed building is evaluated to assess the change of trend after event. Then, an omnibus test is used to assess changes across the time series: polarimetric SAR data are represented by complex variance-covariance matrices, whose homogeneity is evaluated through a factorization of multiple independent likelihood ratio tests in the time series. To determine where and when a change has occurred in our time series, we implemented a sequential omnibus tests algorithm assessing the overall differences between distributions at multiple times. We obtain temporal change maps that allow to represent the timeline of occurrences of change.

The results of the first analysis show deviations in building's temporal signatures, for each orbit and polarization. For the evaluation of the temporal change maps, we infer the cause of the change related to the event using our building datasets to measure the performance of our model. Then, we performed a sensitivity analysis of this evaluation for orbits 116 Ascending and 21 Descending over both building datasets and for different levels of significance.

Depending on the priority of risk assessment, the multitemporal map, avoiding pixels where changes occurred, is more interesting with its high specificity compared to the bitemporal map. Regarding the relatively high missing rate from the map of first change, the use of frequency of changes would have been interesting to filter pixels prone to frequent changes. However, these results are highly side-looking data-driven and method-dependent for performance evaluation. They could be enhanced with adding polarimetric features, phase information from SLC data, and more advanced change detection techniques.

The process is developed on Google Earth Engine via a Colaboratory Notebook *available here*, linked with a Github repository hosting and sharing the reference data. The outputs of both analysis are displayed via an interactive HQ Observable platform *available here*, offering insights into the strengths and limits of each approach at the building level across various parameters. The integration of temporal signatures, statistical change detection, and interactive visualization aids in a comprehensive understanding of the spatial and temporal distribution of building damage. It provides a benchmark for the unsupervised intensity-based approach and allows more informed discussions on future model strategies for post-disaster recovery.

---

## Résumé

Evaluer les impacts d'un séisme est crucial pour fournir efficacement des informations aux services d'urgence et pour la phase de reconstruction. À cet égard, les séries temporelles d'images radar offrent de nombreux avantages pour évaluer les dégâts aux bâtiments. Ce mémoire explore une méthode de détection de changement multi-temporelle et non-supervisée pour évaluer, à l'aide d'images Sentinel-1, les dégâts aux bâtiments suite au séisme en Turquie en Février 2023.

Avant tout, un dataset de bâtiments détruits est construit à partir de l'examen des produits du CEMS, par analyse visuelle d'images optiques avant et après le désastre. Une série temporelle de l'intensité moyenne du signal renvoyé pour l'emprise de chaque bâtiment est analysée afin d'analyser la signature avant/après événement. Ensuite, un test omnibus est utilisé pour évaluer les changements au sein de la série temporelle: les données SAR polarimétriques sont représentées par des matrices de covariance complexes, dont l'homogénéité est évaluée par une factorisation de plusieurs tests de rapport de vraisemblance indépendants dans la série temporelle. Pour déterminer où et quand un changement est détecté, nous utilisons un algorithme séquentiel de tests omnibus qui évalue les changements entre distributions à plusieurs dates. Nous obtenons des cartes du premier changement, du plus récent, et de leur fréquence.

Les résultats de la première analyse montrent des écarts significatifs dans les signatures temporelles, pour chaque orbite et chaque polarisation. Ensuite, pour évaluer les performances de notre modèle, nous analysons l'impact du désastre en corrélant les changements survenus lors de l'événement avec nos jeux de données de bâtiments détruits ou non. Une analyse de sensibilité de cette évaluation est ensuite réalisée, pour les orbites Ascendante 116 et Descendante 21, sur les deux jeux de données de bâtiments, et pour différents niveaux de significativité.

Dans le contexte de la gestion des risques, la carte multitemporelle du premier changement, filtrant les pixels où des changements sont déjà survenus, est plus intéressante pour sa spécificité comparé à la carte bitemporelle. Le taux relativement élevé d'omissions sur la carte du premier changement amène à considérer l'utilisation de la fréquence des changements pour filtrer les pixels sujets à des changements fréquents. Cependant, ces résultats dépendent fortement des propriétés des images SAR et des méthodes d'évaluation utilisées. Ils pourraient être améliorés par l'ajout de la phase provenant des données SLC et le recours à des techniques de détection de changements plus avancées.

Le processus est développé sur Google Earth Engine via un notebook Colaboratory *disponible ici*, relié à un dépôt Github hébergeant et partageant les données de référence. Les résultats de nos deux analyses sont présentés *via une plateforme interactive* qui permet d'observer les forces et limites de chacune, à l'échelle des bâtiments et pour différents paramètres. La visualisation interactive des signatures temporelles et des cartes temporelles contribue à une compréhension approfondie de la distribution spatiale et temporelle des dommages aux bâtiments. Cela fournit un point de référence pour les futures modèles relatifs au sujet, d'une approche non supervisée et basée sur l'intensité.

---

## Contents

<b>1</b>	<b>Introduction</b>	<b>8</b>
<b>2</b>	<b>Fundamentals of radar imagery</b>	<b>10</b>
2.1	Basics of radar imagery . . . . .	10
2.1.1	Side Looking and SAR . . . . .	10
2.1.2	Signal properties . . . . .	12
2.1.3	Geometric properties of SAR data . . . . .	13
2.1.4	Radiometric properties of SAR data . . . . .	13
2.2	Sentinel-1 Case . . . . .	16
2.2.1	Sentinel-1 images statistical properties . . . . .	17
<b>3</b>	<b>State of the Art</b>	<b>18</b>
3.1	Mono- and Multitemporal techniques . . . . .	18
3.2	Intensity-based Change Detection . . . . .	18
3.3	Coherence-based change detection . . . . .	22
<b>4</b>	<b>Research Question</b>	<b>23</b>
<b>5</b>	<b>Method</b>	<b>24</b>
5.0.1	Theoretical concepts . . . . .	26
5.1	Data pre-processing . . . . .	30
5.1.1	Production of a building footprint dataset . . . . .	30
5.1.2	Sentinel-1 Images Dataset . . . . .	36
5.2	Intensity temporal signatures of Destroyed building . . . . .	37
5.3	Multitemporal change detection . . . . .	37
5.3.1	The omnibus test statistic . . . . .	37
5.3.2	The sequential omnibus change detection . . . . .	38
<b>6</b>	<b>Results</b>	<b>39</b>
6.1	Intensity temporal signatures of Destroyed building . . . . .	39
6.2	Multitemporal change detection . . . . .	41
6.2.1	The omnibus test statistic . . . . .	41
6.2.2	The sequential omnibus change detection . . . . .	42
<b>7</b>	<b>Discussion</b>	<b>49</b>
7.1	Regarding the research objective . . . . .	53
7.2	About event-related works . . . . .	54
7.3	Limits and perspectives . . . . .	54

---

<b>8 Conclusion</b>	<b>57</b>
<b>Bibliography</b>	<b>59</b>
<b>Appendix</b>	<b>63</b>

---

## List of Figures

Figure 1 Observation geometry of a SLAR imager . . . . .	10
Figure 2 Geometry of observations used to form the synthetic aperture for target . . . . .	11
Figure 3 Illustration of different SAR operation modes . . . . .	11
Figure 4 The dependence of surface roughness on the sensor wavelength. . . . .	12
Figure 5 Main geometric distortions on SAR images . . . . .	13
Figure 6 Different polarizations and scattering strength across different surfaces . . . . .	14
Figure 7 Illustration of the multiplicative character of speckle. . . . .	14
Figure 8 Sentinel-1 operational modes . . . . .	16
Figure 9 Ideal scattering from a flat-roof building including . . . . .	19
Figure 10 Backscattering range profile from flat roof building with different heights . . . . .	19
Figure 11 Backscattering range profile from steep roof with different incident angles . . . . .	19
Figure 12 Optical and VHR SAR view of a flat-roof building still intact . . . . .	20
Figure 13 Comparison of optical and VHR SAR views from intact and damaged building, . . . . .	21
Figure 14 Overview of our methodological framework . . . . .	25
Figure 15 Schema of the visual analysis process . . . . .	32
Figure 16 Overview of <i>Cases</i> encountered during review of CEMS products. . . . .	34
Figure 17 Sentinel-1 Images Collections Imprints covering our AOIs (red) . . . . .	36
Figure 18 Intensity (dB) temporal signature for footprint with OSM ID 352308002 . . . . .	39
Figure 19 Intensity (dB) temporal signature for footprint with OSM ID 222765255 . . . . .	39
Figure 20 Histograms of values from omnibus tests performed simultaneously . . . . .	41
Figure 21 Multitemporal change maps for Kahramanmaras (AOI4) . . . . .	43
Figure 22 Comparison of temporal signatures and start map for various footprints. . . . .	50
Figure 23 Start maps for each orbit and temporal signatures of buildings with few changes . . . . .	51
Figure 24 Disaster impact at buildings level seen with WV02 image . . . . .	51
Figure 25 Start maps ( <b>smap</b> ) of first change . . . . .	52
Figure 26 WV02 image from (12/02/23) for industrial zone and corresponding buildings. . . . .	52
Figure 27 Surface deformation of the EAFZ seismogenic faults . . . . .	B 1
Figure 28 Commonly used radar wavebands and frequency associated. . . . .	B 2
Figure 29 Polarization settings define how waves are transmitted and received. . . . .	B 2
Figure 30 From SLC to GRD product (ESA, 2024). . . . .	B 3
Figure 31 Informations from CEMS ready-to-use map for AOI01 . . . . .	B 4
Figure 32 CEMS methods description . . . . .	B 5
Figure 33 Explanation of CEMS naming convention . . . . .	B 5

---

Figure 34 EMSR648 Activation Extent Map from CEMS. . . . .	B 6
Figure 35 Bitemporal map of changes detected During event for each AOI. . . . .	B 8
Figure 36 Bitemporal map of changes detected Before event for each AOI. . . . .	B 9
Figure 37 Map of first occurrence of change During event for each AOI. . . . .	B 10
Figure 38 Map of first occurrence of change Before event for each AOI. . . . .	B 11
Figure 39 Definitions of metrics. . . . .	B 12
Figure 40 Temporal signatures of buildings in industrial zone with increasing trend. . . .	B 13

---

## List of Abbreviations

- AOI... Area of Interest
- CEMS... Copernicus Emergency Management Service
- EAFZ... East Anatolian Fault Zone
- EDV... Earthquake Damage Visualization
- EO... Earth Observation
- GEE... Google Earth Engine
- GLCM... Gray Level Co-occurrence Matrix
- GIS... Geographic Information System
- GRD... Ground Range Detected
- InSAR... Interferometric Synthetic Aperture Radar
- IW... Interferometric Wide Swath
- LRT... Likelihood Ratio Test
- OSM... OpenStreetMap
- PolSAR... Polarimetric Synthetic Aperture Radar
- RADAR... RAdio Detection And Ranging
- RGB... Red, Green, Blue
- RS... Remote Sensing
- SAR... Synthetic Aperture Radar
- SLAR... Side-Looking Airborne Radar
- SLC... Single Look Complex
- TOPSAR... Terrain Observation by Progressive Scans SAR
- UAV... Unmanned Aerial Vehicle
- UNITAR... United Nations Institute for Training and Research
- VHR... Very High Resolution
- WGS... World Geodetic System

---

## 1. Introduction

Earthquakes are one of the most frequent and destructive natural disasters that affect mankind. They result from sudden energy releases in the earth's crust, creating seismic waves which result in ground shaking. They are usually caused by slippage on a seismic fault due to built-up friction between tectonic plates. In 2023, two major devastating earthquakes in Turkey, followed by another in Morocco, led to significant humanitarian disasters. This study focuses on the event in Turkey, which impacted East Anatolia on 6 February 2023. Two consecutive seismic events with magnitude  $>Mw7.0$  occurred consecutively in the western section of the East Anatolia Fault Zone (EAFFZ), between the Anatolian and Arabian Plates (Fig. 27 in Appendix). Two quakes occurred at 4:17 am and 1:24 p.m. with epicenters located in Provinces of Kahramanmaraş (37.47E, 37.56N at a depth of 15 km) and of Gaziantep (37.22E, 38.11N at a depth of 12 km). With 96 km apart, they are the "double shock earthquake" in the swarm earthquake (Wang et al., 2023). The first quake, called the "main shock" is followed by a second one equally strong or slightly weaker, "the after shock". This phenomenon can cause more significant damage because the first event weakens structures, and the second shock exacerbates the destruction.

Their occurrence is often accompanied by huge loss of lives, especially at night, and damage to properties. During the 21st century, around 0.78 million people lost their lives in seismic disasters, with an average of 32,513 fatalities per year (Macchiarulo et al., 2024). The Turkish event was one of the strongest to hit the country in over 100 years and resulted in around 58,000 lives lost. It also led to 34.2 billion\$ in direct damage. One year later, many families have still not been rehoused. Moreover, rapid urbanization increases the risk of earthquake-induced damages in urban areas (Dong & Shan, 2013). For example in southern Turkish cities, most buildings have unreinforced brick masonry structures and low-rise concrete frames (Arslan Kelam et al., 2022).

In response to such catastrophic events, impact assessment is crucial for effective search and rescue operations, especially in the immediate aftermath when time is crucial for saving lives (Du et al., 2024). Timely acquisition of damage information is essential to minimize casualties as people trapped in collapsed buildings can generally survive for 48 h maximum (Ge et al., 2020). Since most casualties are primarily related to building collapses, accurate assessment of the impact in terms of the damage sustained by built assets and the associated loss plays a vital role (H. Liu et al., 2024). The selection of a particular approach for damage and loss evaluation typically involves a trade-off between the level of details collected and the timeliness of evaluation (Rao et al., 2023). The first step in emergency response is to assess the area extent concerned by the disaster (Arai et al., 2024) and the impact level of the damage (Mazzanti et al., 2022). It is also important to detect which transport infrastructure are still intact to be used for the crisis support (Plank, 2014).

Rapid Mapping is defined by CEMS as “the on-demand and fast provision of geospatial information in support of emergency management immediately following an emergency event”. Conducting field surveys after a disaster is often challenging and can be dangerous, with damaged infrastructure possibly limiting timely on-site assessments (Ge et al., 2020). Thus, remote sensing have contributed significantly to support the management of disaster situations, owing to their renowned attributes of efficiency, convenience, and accuracy (Du et al., 2024). Space-borne sensors enable the monitoring of a wide area with a regular revisit time (several days, depending on the orbit altitude). Satellites have the great advantage of fast response capabilities and some can be operated in a ‘Spotlight Mode’, which allows to point the radar beam at a precise area, for specific high-resolution requests like disaster events. The amount, timeliness, and availability of satellite imagery covering a crisis situation improved substantially the last fifteen years (Voigt et al., 2007). Several authors reviewed the use of remote sensing for disaster management support (Dong & Shan, 2013; Joyce et al., 2009). Research shows that remotely-sensed data can provide valuable information at each stage of the comprehensive disaster management cycle (Ge et al., 2020; Kaku, 2019).

Sensors used for earthquake damage assessment are quite diverse, in terms of spectral resolution and frequency. Most applications of disaster response based on optical satellite images rely on the visual interpretation of optical images by trained operators that manually tag building damage assessment (Matin & Pradhan, 2022). It remains the most reliable and independent method for evaluating automated techniques, often serving as the benchmark for validating results (Dong & Shan, 2013). However, such task is time-consuming, inconvenient for large areas, requires trained operators and generates a heavy workload, making it unsuitable to asses rapid mapping over an extensive area (Dong & Shan, 2013). Moreover, optical images from satellites are only available during daytime and for days without cloud cover. Similarly, UAVs can be challenged by weather conditions such as strong winds or rain, and require presence of both trained personnel with specialized equipment (Malmgren-Hansen et al., 2020).

Among the different kinds of EO systems, radar is of great value for the emergency mapping, as imaging at microwave wavelengths is irrespective of any weather or lighting conditions and exploiting nighttime passes increases the revisiting time (Ajmar et al., 2015). Radar imagery contains useful detailed amplitude and complex information, supporting both change detection and surface deformation analysis (Wang et al., 2023). The launches of several radar systems over the past ten years have made it more common to use radar data, and particularly the time series. Since the constellation of Sentinel-1A and 1B entered service in 2014 and 2016 respectively, a large number of free medium-resolution images with wide coverage, rich archived data, short-time baselines, and high orbital accuracy can serve disaster emergency response and allow multitemporal analyses (Plank, 2014). Therefore, we will focus our study on damage assessment using multitemporal Sentinel-1 data.

## 2. Fundamentals of radar imagery

### 2.1. Basics of radar imagery

To understand how to extract information from radar images, we first introduce some basic principles and refer to Moreira et al. (2013) and Flores-Anderson et al. (2019) for more insights.

#### 2.1.1. Side Looking and SAR

Radar imagery involves transmitting electromagnetic microwaves and receiving a portion of the echoes that are scattered back from the Earth's surface. Radar systems do so by side-looking to differentiate angles and distances to objects. The antenna is pointed away from nadir by a look angle  $\theta_l$  lighting a continuous swath on the ground range direction as the craft moves along.

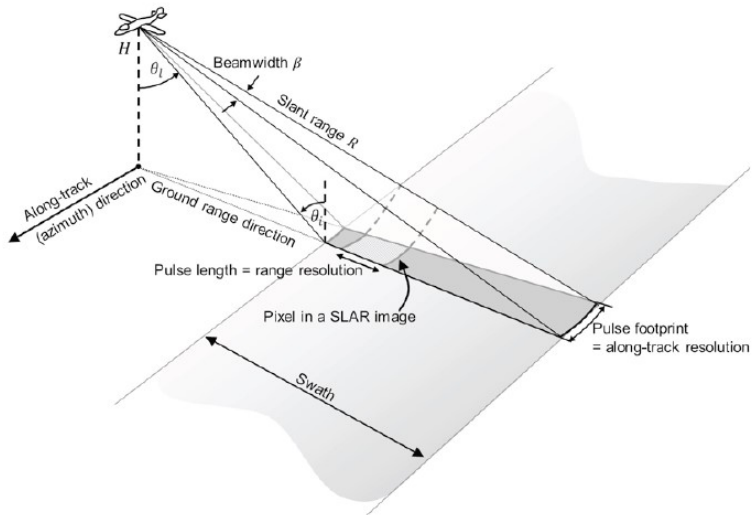


Figure 1: Observation geometry of a SLAR imager from altitude  $H$  observing at an oblique look angle  $\theta_l$ . The size of the illuminated footprint is determined by the beamwidth  $\beta$  and the slant range  $R$  (Flores-Anderson et al., 2019).

While flying along its track (azimuth direction), the radar system is transmitting a sequence of short microwave pulses. Each pulse covers an area on the ground referred to as the antenna footprint (see darker gray area in Fig. 1). The size of this footprint in either the range or azimuth direction is defined by the relationship between system wavelength  $\lambda$ , the side length  $L$  of the antenna along this direction, and the distance of the radar sensor from the ground  $R$ :

$$\text{Surface Footprint} \approx \frac{\lambda}{L} R = \beta \cdot R \quad (2.1)$$

with  $\beta$  defining the antenna's beamwidth through  $\beta = \lambda/L$ .

To simulate a large antenna aperture and achieve higher spatial resolution, Synthetic Aperture Radar (SAR) systems use the motion of the radar antenna. This principle uses the consecutive transmission/reception times which translate into different positions due to platform movement (Fig. 3). An appropriate coherent combination of the received signals along its flight line allows the synthesis of a virtual aperture much longer than the physical antenna length. The very nature of SAR is that the return echoes from the illuminated scene are sampled both in range and azimuth.

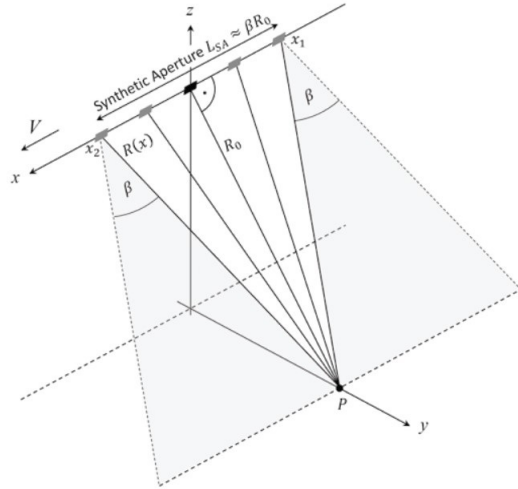


Figure 2: Geometry of observations used to form the synthetic aperture for target P at along-track position  $x = 0$  (Flores-Anderson et al., 2019).

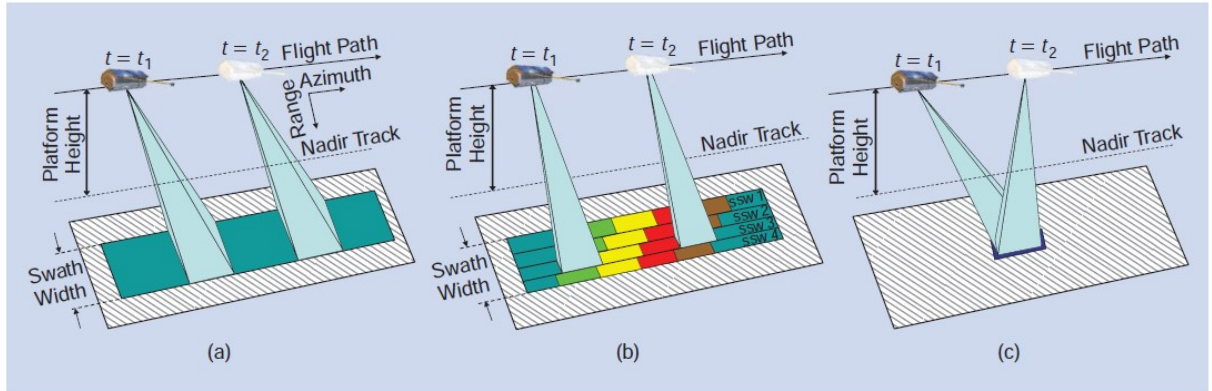


Figure 3: Illustration of different SAR operation modes which are used to increase the swath width (b: ScanSAR) or improve the azimuth resolution (c: Spotlight) compared to the Stripmap mode (a) (Moreira et al., 2013).

### 2.1.2. Signal properties

Radar systems measure both amplitude (strength) and phase (timing) from the backscattered echo signal, which are then represented as a two-dimensional data matrix of complex signals. The first dimension of the data matrix corresponds to the range direction while the second dimension is known as azimuth or slow-time. Each complex signal ( $S$ ) is expressed in terms of its real and imaginary parts, based on amplitude ( $A$ ) and phase ( $\varphi$ ):

$$S = Ae^{i\varphi} = A \cos \varphi + iA \sin \varphi \quad (2.2)$$

Amplitude indicates the signal strength upon returning to the radar sensor, helping determine target characteristics like surface roughness and material type. The intensity is the square of the amplitude :

$$I = A^2 = Re^2 + Im^2 \quad (2.3)$$

with  $Re$  and  $Im$  representing the real and imaginary part of the complex SAR value. Radar imagery capture signals that vary over several orders of magnitude, therefore data are often expressed in a logarithmic unit, decibels (dB). Phase indicates the relative value of the echo waves in a full period and reflects the distance traveled by the signal. These properties are influenced by the imaging geometry of the SAR sensor (orbit direction, incidence angle and polarization) as well as by the physical (i.e., geometry, roughness Fig. 4) and dielectric properties (i.e., permittivity) of the imaged object (Moreira et al., 2013).

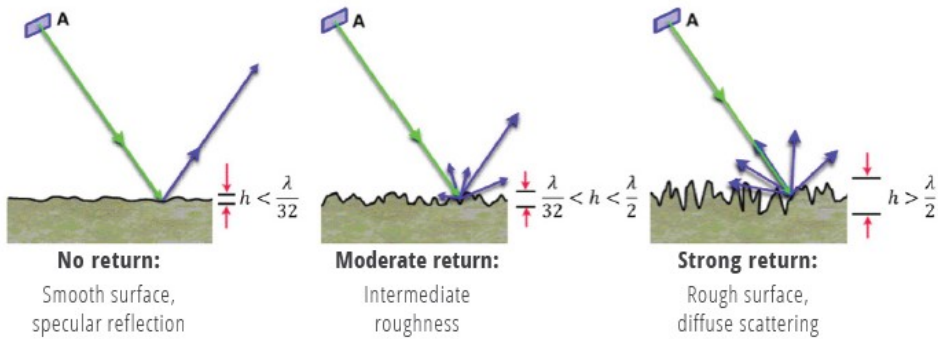


Figure 4: The dependence of surface roughness on the sensor wavelength (Flores-Anderson et al., 2019).

### 2.1.3. Geometric properties of SAR data

Due to the oblique observation geometry inherent to all imaging radar systems, surface slopes and similar terrain features lead to geometric distortions in data acquired by SAR systems. The origins and main characteristics of these distortions are summarized in Figure 5. This is a key concept for building damage assessment, which has been widely studied (see Chapter 3). Hence, topography-related distortions cannot be entirely removed, and image acquisitions from more than one point of view may be necessary to minimize all three imaging effects.

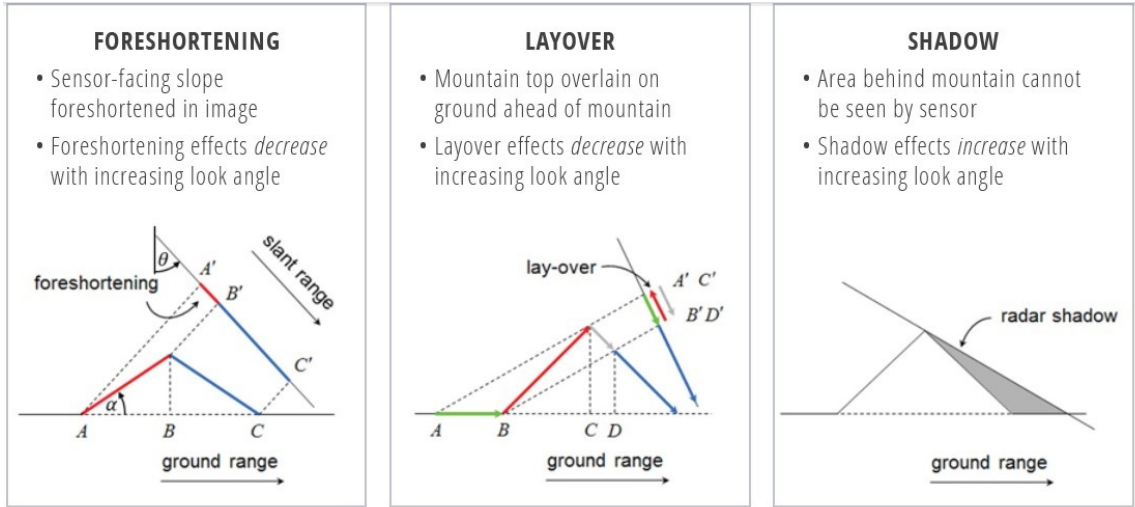


Figure 5: Main geometric distortions on SAR images with their dependence on acquisition geometry: (a) foreshortening, (b) layover, and (c) shadow (Moreira et al., 2013).

### 2.1.4. Radiometric properties of SAR data

As active systems, SAR instruments allow full control over the transmitted and received signal polarizations (PolSAR), which describe the orientation of the electric field vector in the plane orthogonal to the wave propagation direction (see Fig. 29 in Appendix). Single polarization mode involves the application of only one type of polarization, typically either HH or VV. Dual-pol systems, like Sentinel-1, can additionnally transmit in one orientation (horizontal H or vertical V) and receive in the other orientation (VH or HV). The polarization features are sensitive to dielectric constants, physical properties, geometry, and the orientation of ground targets (Ge et al., 2020). Understanding how polarization interacts with ground objects is crucial, as different settings result in varying radar brightness depending on the scattering types (Fig. 6). In urban areas, double bounce scattering occurs when the pulse reflects off two perpendicular surfaces, resulting in a particularly strong returned signal due to multiple energy transmissions back to the sensor. This results in co-polarized (VV or HH) echoes being higher in urban areas compared to cross-polarized echoes (VH or HV) (see Fig. 6).

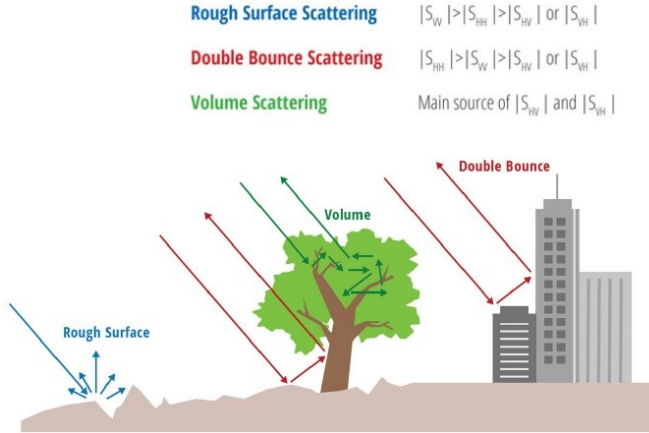


Figure 6: Different polarizations lead to varying scattering strength across different surfaces (Flores-Anderson et al., 2019).

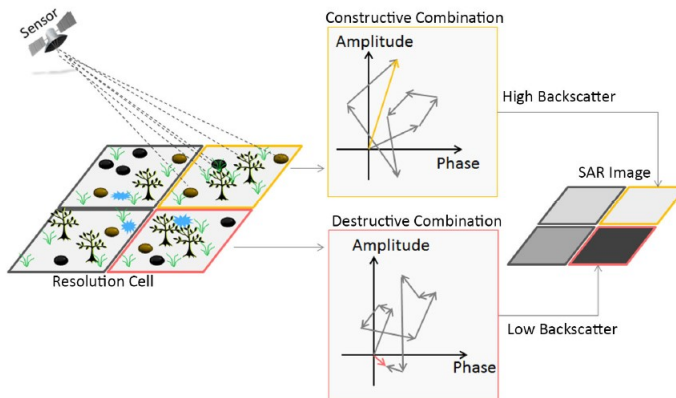


Figure 7: Illustration of the multiplicative character of speckle. The variations observed caused by speckle are strongly correlated to the intensity (Salepci et al., 2017).

SAR images are characterized by speckle effect. It is caused by the random distribution of many scatterers within a resolution cell resulting in the salt-and-pepper appearance of SAR imagery. The coherent sum of their amplitudes and phases leads to strong fluctuations in the backscattering (Fig. 7). Consequently, the intensity and the phase are no longer deterministic, but instead follow an exponential and uniform distribution, respectively (Moreira et al., 2013). Speckle is a true electromagnetic measurement, although it is commonly referred to as noise: it cannot be reduced by increasing the transmit signal power, since it has a multiplicative character - its variance increases with its intensity (Moreira et al., 2013). A technique called multilook is used to reduce speckle in SAR images by averaging multiple independent looks of the same area. Each look is obtained by dividing the original SAR data into sub-images that are processed separately and then averaged.

Thus, analyzing PolSAR images requires tailored image processing based on the complex information, the statistical properties of speckled data and taking in account the multilooking process (Nascimento et al., 2018).

PolSAR theory states that scattering behavior of targets in different polarizations is represented by a complex scattering matrix given by :

$$\begin{pmatrix} E_v^r \\ E_h^r \end{pmatrix} = \frac{e^{-irk}}{r} \begin{pmatrix} S_{vv} & S_{vh} \\ S_{hv} & S_{hh} \end{pmatrix} \begin{pmatrix} E_v^t \\ E_h^t \end{pmatrix}^* \quad (2.4)$$

where

- the transmitted polarized radar signal  $E^t$  (decomposed horizontally and vertically) is transformed by the complex scattering matrix [S] into the backscattered signal  $E^r$ .
- the exponent term accounts for the phase shift due to the return distance  $r$  from target to sensor, where  $k$  is the wave number  $k = 2\pi/\lambda$ .
- the \* denotes complex conjugation
- each element  $S_{ij}$  is a complex number that contains both amplitude and phase information (cf Eq. 2.2), representing how the signal is scattered for different polarizations.

From measurement of the returned signal, two of the four complex scattering matrix elements can be derived and processed into two-dimensional (slant range  $x$  azimuth) arrays mentioned above 2.1.2, comprising the so-called Single Look Complex image (Canty, 2024).

Written as a complex vector, the two derived elements are  $S = \begin{pmatrix} S_{vv} \\ S_{vh} \end{pmatrix}$ . The outer product of  $S$  with its complex transpose  $\begin{pmatrix} S_{vv}^* & S_{vh}^* \end{pmatrix}$  is the (dual pol) covariance matrix image:

$$S = \begin{pmatrix} S_{vv} \\ S_{vh} \end{pmatrix} \begin{pmatrix} S_{vv}^* & S_{vh}^* \end{pmatrix} = \begin{pmatrix} |S_{vv}|^2 & S_{vv}^* S_{vh} \\ S_{vh}^* S_{vv} & |S_{vh}|^2 \end{pmatrix} \quad (2.5)$$

The diagonal elements are real numbers, the off-diagonal elements are complex conjugates of each other and contain the relative phases of the  $S_{vv}$  and  $S_{vh}$  components. The components containing both co- and cross-polarized often contain little information, so for randomly distributed targets with azimuthal symmetry, those off-diagonal elements are zero.

Measuring the full scattering matrix allows to build up a powerful observation space sensitive to shape, orientation and dielectric properties of the scatterers and allows the development of physical models for the identification of scattering mechanisms occurring inside the same resolution cell (Moreira et al., 2013).

## 2.2. Sentinel-1 Case

Sentinel-1 is a European Space Agency satellite mission started in 2014. It was designed as a constellation of two sun-synchronous polar-orbiting satellites (1A launched in 2014 and 1B in 2016), sharing the same orbital plane with 180° orbital phasing difference, performing C-band synthetic aperture radar imaging (see Fig. 28 in Appendix). In December 2021, Sentinel-1B has been declared inapt due to an instrument anomaly, leaving Sentinel-1A in charge with a 12 days revisit time instead of 6 with both satellites. Meaning it is able to map the entire world in the Interferometric Wide (IW) swath mode once every 12 days, with 175 orbits per cycle. It operates in four exclusive imaging modes (Fig. 8) with different resolution (down to 5 m) and coverage (up to 400 km). It provides dual polarisation capability and rapid product delivery.

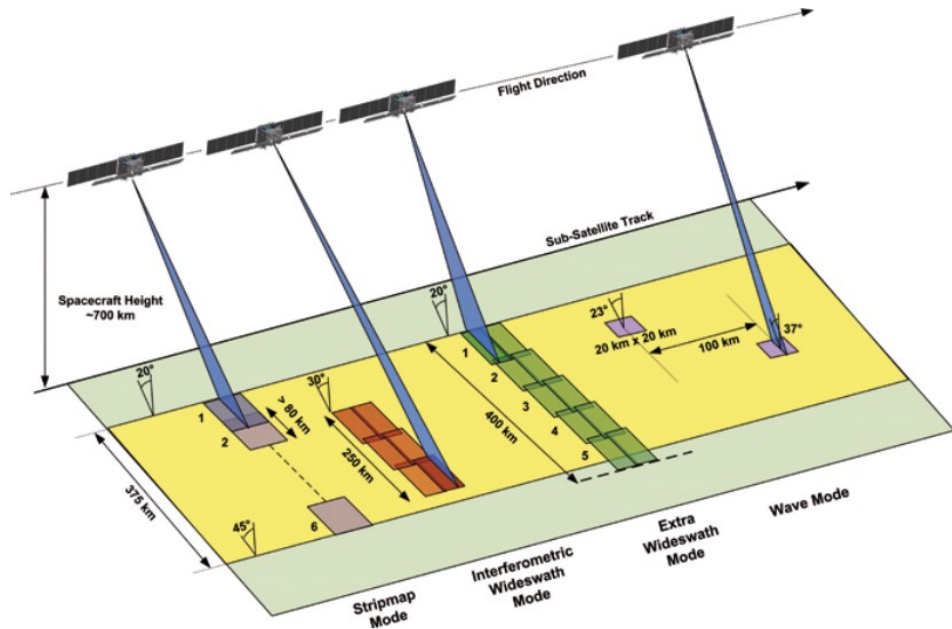


Figure 8: Sentinel-1 operational modes (ESA, 2024).

The IW swath mode is the main acquisition mode over land. To meet the demanding image quality and swath width requirements, the IW mode is implemented as a ScanSAR mode with progressive azimuth scanning. It captures three sub-swaths (Appendix Fig.30a ) using Terrain Observation with Progressive Scans SAR (TOPSAR). With the TOPSAR technique, in addition to steering the beam in range as in ScanSAR, the beam is also electronically steered from backward to forward in the azimuth direction for each burst, avoiding scalloping and resulting in homogeneous image quality throughout the swath. For each mode, products are distributed at three levels of processing, Level-0 for raw data, Level-1 Single Look Complex (SLC) or Ground Range Detected GRD (as well as Level-2 OCN for ocean applications).

### 2.2.1. Sentinel-1 images statistical properties

**SLC products** retain full resolution and phase information in slant-range geometry. The pixels are about 20m x 4m (azimuth range) in extent and the swath widths are about 250km. Dual polarisation Level-1 SLC products contain complex values: in addition to the backscatter intensity that can be measured from each single polarisation, the inter-channel phase information allows to perform enhanced analysis of backscattering properties. Developing Eq. 2.2 for single polarization transmission and reception, e.g., vertical-vertical (*vv*), the received SLC signal can be modeled addressing the real and imaginary parts:

$$S_{vv} = \frac{|S_{vv}^a|}{\sqrt{n}} \sum_{k=1}^n e^{i\phi_k} = \frac{|S_{vv}^a|}{\sqrt{n}} \left( \sum_k \cos \phi_k + i \sum_k \sin \phi_k \right) = \frac{|S_{vv}^a|}{\sqrt{n}} (x + iy) \quad (2.6)$$

and follows an exponential distribution.  $|S_{vv}^a|$  is the overall amplitude characterizing the signal scattered from the area covered by a single pixel.

The effects of randomly distributed scatterers add coherently and introduce a change in phase of the received signal. This is indicated by the sum term in the above equation where  $n$  is the number of elemental scatterers within the resolution cell. The effect varies from pixel to pixel and gives rise to speckle.

**GRD products** are multi-looked, projected onto ground range using the Earth ellipsoid model WGS84 and corrected, containing only amplitude information with reduced spatial resolution (Appendix Fig.30b). For the multi-looking procedure, five cells are incoherently averaged in the range direction to reduce speckle and achieve 20x20m resolution. The pixels are then resampled to 10x10m<sup>2</sup>. In Sentinel-1 multi-look images, the intensity values  $\langle s \rangle = \langle |S_{vv}|^2 \rangle$  or  $\langle |S_{vh}|^2 \rangle$  are obtained by averaging multiple independent, exponentially distributed measurements  $s$  summed over  $m$  looks to give  $\sum_{i=1}^m s_i$ , resulting in a gamma distribution:

$$p(s | a) = \frac{1}{(a/m)^m \Gamma(m)} s^{m-1} e^{-sm/a} \quad (2.7)$$

- with the look-averaged image  $\langle s \rangle = \frac{1}{m} \sum_{i=1}^m s_i$ , written  $s$  for simpler notation;
- and  $a = \text{mean}(\langle s \rangle) = \frac{1}{m} \sum_{i=1}^m \text{mean}(s_i)$  is the mean intensity value.

With  $z = \frac{2sm}{a}$ , we obtain the probability density function of a Sentinel-1 IW\_GRD image, transformed as a chi-square distribution with  $2m$  degrees of freedom :

$$p(z | a) = \frac{1}{2^m \Gamma(m)} z^{m-1} e^{-z/2} \quad (2.8)$$

This distribution will help to model Sentinel-1 image intensity values and perform statistical tests based on hypothesis about images distribution in chapter 5.3 .

---

### 3. State of the Art

This chapter presents some of the studies about building damage assessment using radar imagery. After introducing mono- and multi-temporal techniques, we discuss intensity and coherence-based methods. For each section, we present results from methods applied to the East Anatolia 2023 event.

#### 3.1. Mono- and Multitemporal techniques

The principal advantage of methods using only post-event data is that damage detection can be conducted without reference data which would be suitable for fast initial damage evaluation and rapid response. The downside is a less satisfactory detection outcome given the difficulty in identifying damage without knowing what existed before the earthquake. According to Dong and Shan (2013), the casualties tend to be underestimated when only post-event images are available. Using pre-event GIS data would be a first step to avoid this downside. When such products may be unavailable in developing regions, where the death toll is highest, collaborative mapping like OpenStreetMap (OSM) can provide open-source information (Cooner et al., 2016).

Multitemporal techniques are called change detection, a process of identifying differences in the state of an object by observing the pre- and post-event data (Cooner et al., 2016). Compared to methods using only post-event data, more accurate results can be obtained by using both timelines. Challenges remain in fitting homogeneous pairs of pre- and post-event images (especially with VHR spaceborne systems for which the availability of high-resolution data is often scarce). Co-registration must be addressed to perform automated change detection for two temporal images with different imaging parameters (Dong & Shan, 2013).

#### 3.2. Intensity-based Change Detection

The principle of building damage assessment based on radar intensity changes is as follows: owing to the side-looking of the SAR sensor, an intact building usually reflects four different zones (the layover area, corner reflection, roof area, and shadow area). Figure 9 illustrates the ideal reflection from a flat-roof building and the profiles displaying relative amplitudes of those different scattering zones. It is observed with a 1-m resolution SAR image from TerraSAR-X in Figure 12, viewing a flat-roof building from the left. In parts of areas facing the radar sensor, a bright zone emerges, owing to double bounce effects in corners and the overlying of reflection from the roof, wall, and ground. Hence, edge properties are widely studied in change detection. Dong and Shan (2013) used three machine learning classifiers to extract the features of a building footprint and obtain overall accuracy above 80% for each method. In most building footprint areas and parts of areas facing backward to the radar sensor, a shadow zone appears, owing

to the occlusion of the building. Depending on the incident angle (Fig. 10) or the height of the building (Fig. 11), the layover area can reflect more signal and the shadow area will vary accordingly. Flat roofs reflect less signal toward the sensor compared to gable roofs.

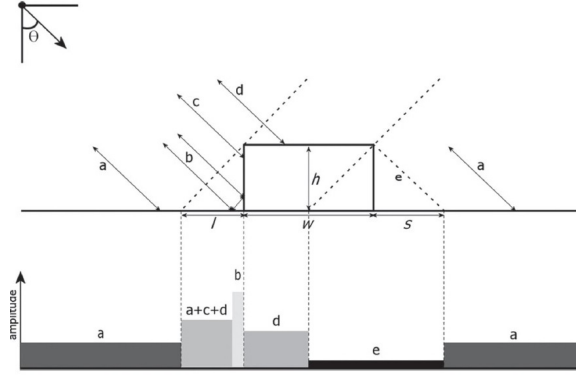


Figure 9: Ideal scattering from a flat-roof building including: ground scattering  $a$ ; double bounce  $b$ ; scattering from vertical wall  $c$ ; backscattering from roof  $d$ ; shadow area  $e$  and  $s$ ; layover area  $l$ . The gray values in the backscattering profiles represent the relative amplitudes (Brunner et al., 2010).

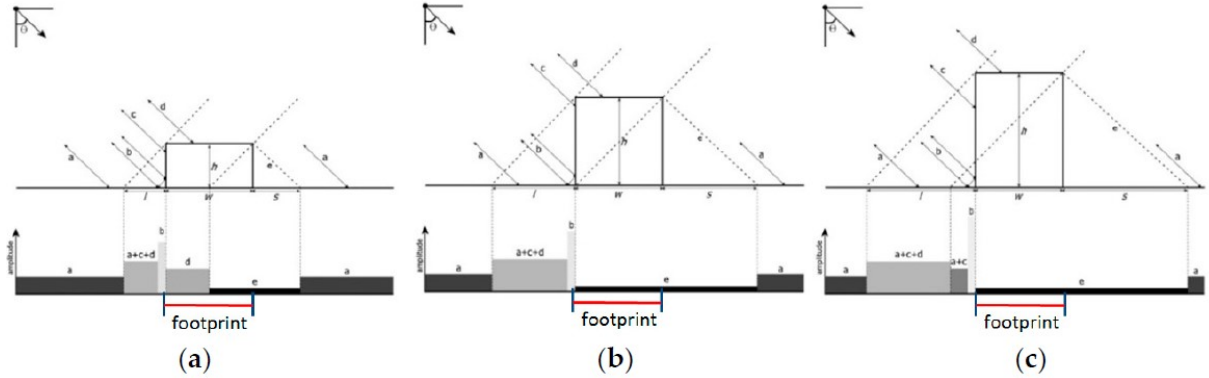


Figure 10: Backscattering range profile from flat roof building varying with different heights (Gong et al., 2016).

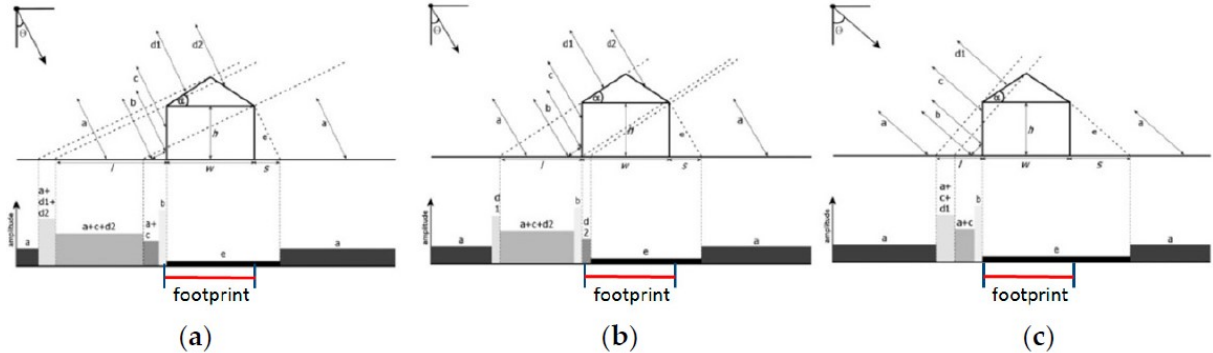


Figure 11: Backscattering range profile from steep roof varying with different incident angles (Gong et al., 2016).

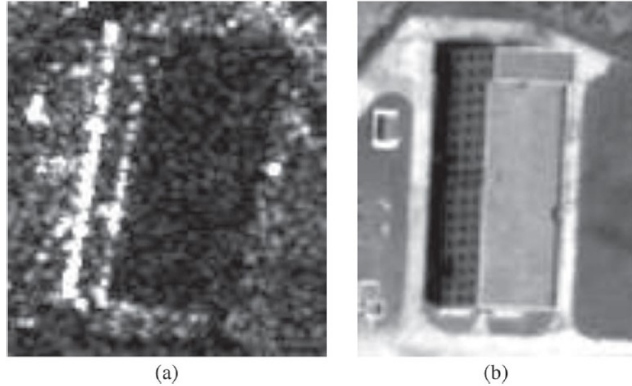


Figure 12: Optical (Quickbird image with 0.6m resolution) and VHR SAR (TerraSAR-X with 1m resolution) views of a flat-roof building still intact (Brunner et al., 2010).

Destroyed buildings have different scattering reflection. This is demonstrated in Figure 13, observing VHR optical and radar images of buildings both intact then damaged. Strong double-bounce scattering may be absent because the vertical wall facing the sensor may be collapsed, and the wall-ground dihedral corner reflector may be destroyed. The layover area may also be missing (though an absence of layover does not necessarily indicate a destroyed building as low buildings lack of it). Furthermore, the shadow area will be reduced or potentially missing, depending on the structure and slope of the ruins (Gong et al., 2016). This will result in a more random and averaged reflection around the building, a smaller amount of specular reflection, of secondary scattering (double bounce), and a considerably larger amount of diffuse reflection signal. Moreover, the scattering mode shifts to anisotropic or multiple scattering (Yang et al., 2024). To sum up, a destroyed building may lack distinct double-bounce, layover, roof or shadow area and exhibits random scattering from the rubble of the collapsed parts, similar to the SAR speckle found in homogeneous regions (Brunner et al., 2010).

Therefore, the urban impacts can be assessed by identifying and quantifying the intensity changes mentioned above through favorable parameters such as intensity difference, correlation coefficient and textures (Ge et al., 2020). Intensity information is relatively easy to access, with no requirement for the acquisition and relatively stable concerning minor changes. A commonly-used method for intensity-based change detection is to calculate the intensity difference and correlation coefficient of the pre- and post-event images and then apply certain thresholds to discriminate building damages (Ge et al., 2020). Generally, the intensity difference becomes high, and correlation coefficient low, as shown by Matsuoka and Yamazaki (2004). In a congested urban context, the radar reflections of damaged areas may be stronger, while for small ratios of building damage in less dense areas, the correlation coefficient ratio are more effective (Ge et al., 2020). Therefore, urban context and disaster severity influences methods results. W. Liu et al. (2018) noticed that correlation coefficients are more sensitive to subtle changes in the ground surface than intensity differences. They also applied the percentage of pixels with decreased

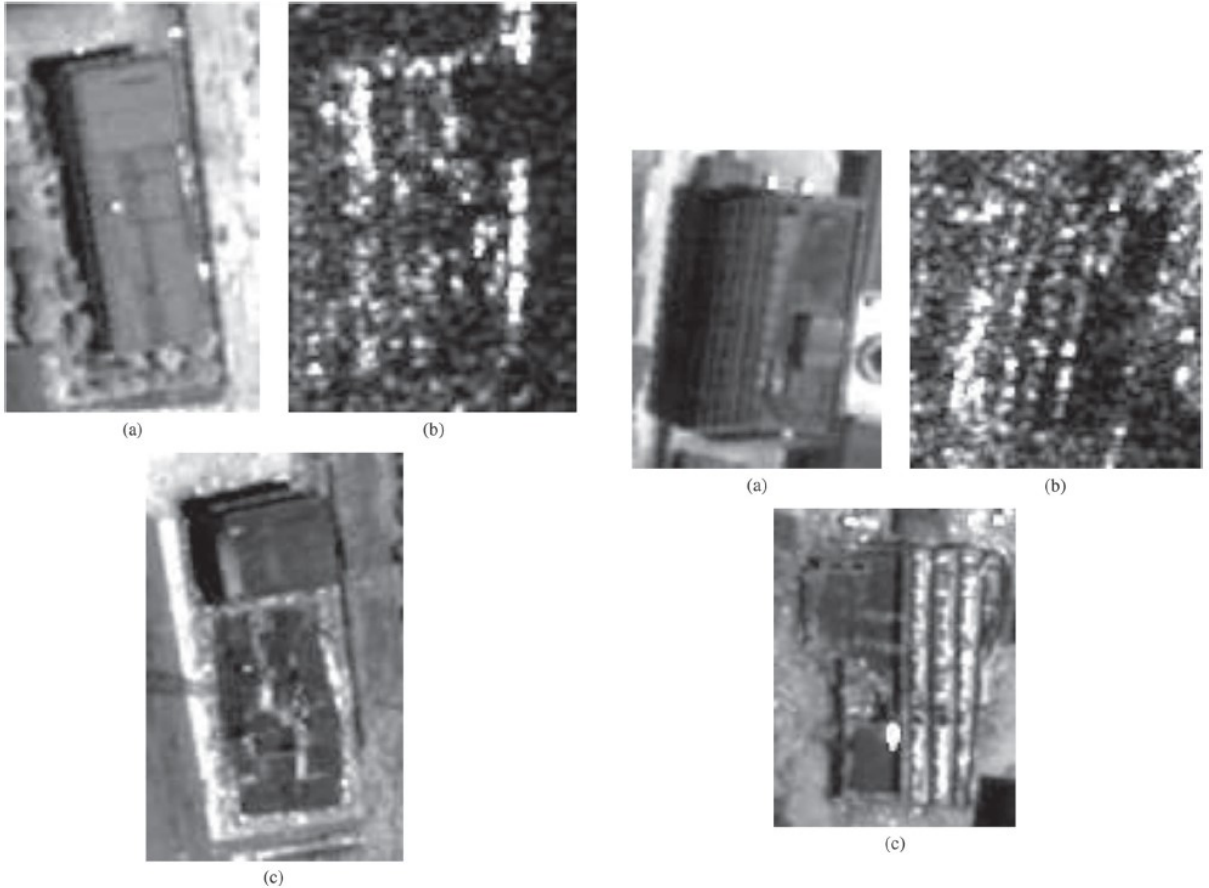


Figure 13: Comparison of optical (a and c) and VHR SAR (b) views from flat-roof buildings, intact (a) and damaged (b and c). Left example shows the building collapsed with two third of and one third standing but damaged. Right example show the building tilted to the side (Brunner et al., 2010).

intensity within walls, and those with increased intensity outside walls, to judge building damage conditions. They also applied the percentage of pixels with decreased intensity within walls, and those with increased intensity outside walls, to judge building damage conditions. However, those methods are specific to a certain level of resolution. At VHR, texture features such as gray level co-occurrence matrixes (GLCMs) to measure the disorder of the reflectivity pattern can be used for building damage assessment (Dell'Acqua & Gamba, 2012). Guida and Brett (2011) also settled a deterministic feature extraction method, based on the double bounce mechanism to identify impacted buildings.

Hence, for the event of East Anatolia in 2023, Macchiarulo et al. (2024) extracted GLCM textural features from solely post-event Capella's VHR SAR imagery and used a random forest model to assess building damages after East Anatolia event. The best performing combined model achieved overall accuracy ranging from 73 to 83%. Yu et al. (2024) also proposed a multi-class damage detection model by random forest classification to combine four variables, from

which the temporal variance in amplitude (ADI). They correlated those with damage severity data from ground truth, to extract each feature importance. With merely a 3% difference in feature importance, the ADI demonstrates good results at the building level, leveraging the 10 m-resolution of ALOS-2 images. The other feature using radar imagery was based on pre- and co-seismic coherence.

### 3.3. Coherence-based change detection

Phase information is exploited with SAR interferometry (InSAR) methods to measure ground deformation and changes of surfaces. It is very sensitive to change in building shape due to seismic effects and can detect moderate casualties. Coherency imagery represents the degree of correlation of phase information between two radar images. Ito et al. (2000) presented damage evaluation results based on coherence imagery showing temporal decorrelation in impacted regions (high coherence indicates little change, while low coherence indicates significant change). After decorrelation analysis, the images obtained by interferometric processing showed that the building damage grade is highly related to the variability index of the coherence coefficient. Sharma et al. (2017) presented an earthquake damage visualization (EDV), merging RGB imagery with indicators calculated through pre- and post-event coherence images. Several additional polarimetry parameters, such as polarization coherence, which can be used to characterize surface roughness and the polarimetric orientation angle having a close relationship with building orientation, were also said to be favorable parameters for understanding damages in built-up areas (Ainsworth et al., 2008; Ge et al., 2020). However, the use of polarimetric data is limited by its low resolution and low sensitivity to damage in buildings that were not aligned with the satellite flight direction (W. Liu et al., 2018). Consequently, these methods were designed for a damage assessment at the city block level rather than at the building level.

Several studies were conducted after the East Anatolia event using InSAR: Du et al. (2024) produced a rapid deformation grading map to address the effectiveness of InSAR in detecting north-south deformation. They observed a gradient of deformation increasing with distance to the epicenter for all buildings at the city scale, though not allowing the detection of precise destroyed buildings. Hence, InSAR is predominantly used in large-scale land subsidence studies (Du et al., 2024). Wang et al. (2023) also used coherence information with Sentinel-1 imagery, and detected around 67% of the destroyed building comparing with the output from Microsoft team using artificial neural network. Also with Sentinel-1 images, H. Liu et al. (2024) proposed a new method based on a multitemporal InSAR coherence that combines a coherence estimation approach based on homogeneous SAR pixels and the histogram matching technique. They obtained the spatial distribution of stable points in the region and removed the information in non-building areas using OSM footprints. Their method performed validation on the East Anatolia event, with a correct rate of 72.8%, 27.2% missing and 13.3% false identification.

---

## 4. Research Question

On one hand, supervised methods rely on the time-consuming labelling of data to train learning models and are dependent on its accuracy. On the other hand, unsupervised change detection approaches, are relatively straightforward, easy to implement or interpret and require no human intervention. However, the results of traditional pixel-based unsupervised change detection methods are also susceptible to speckle noise (Yousif & Ban, 2016), which can result in a high false alarm rate (W. Liu et al., 2018). Thus, analyzing SAR images requires tailored image processing based on the complex information, the statistical properties of speckled data and taking in account the multilooking process (Nascimento et al., 2018).

SAR change detection can be generalized to the stability or change analysis for a whole series of images over a given time range but research on detecting changes in SAR time-series remains limited (Colin, 2023). In this regard, the omnibus likelihood ratio test statistic approach is testing the hypothesis that all polarimetric signals from a time series belong to a single statistical population. This method proved particularly useful in multi-temporal change detection, and can detect both abrupt and steady increased changes (Conradsen et al., 2016). The research group around Nielsen & Conradsen (2016) presented the multitemporal omnibus change detection, along with the further development, to answer various challenges such as flood and wetlands monitoring or deforestation. The method appeared particularly effective in scenarios where man-made targets appear or disappear against a natural background (Canty et al., 2019). Accordingly, Malmgren-Hansen et al. (2020) presented the relevance of this approach for damage assessment after a cyclone, despite not being compared to ground truth damage assessment. Our study adds to the research by presenting this unsupervised multitemporal method to assess building damage related to seismic event. The research objective is:

**Assessing building damage after a seismic event using unsupervised change detection with Sentinel-1 imagery.**

Our study will focus on the seismic event of 2023 in Eastern Anatolia, Turkey.

The stages of the research are :

- to investigate the quality of the operational maps produced by CMES rapid mapping and to produce a reliable dataset of destroyed building;
- to evaluate changes of trend in signal intensity over time for this dataset;
- to assert the multitemporal change detection method's ability to apply to our case;
- to apply the method to determine the timing and extent of damage;
- to explore results in a comprehensive understanding of both approaches regarding different parameters.

---

## 5. Method

This chapter describes the methodology in three parts: the data used and the preparation of our dataset (part 5.1), the extraction of intensity temporal signatures of destroyed buildings footprints (part 5.2), and the multitemporal change detection (part 5.3).

From the review of the CEMS building assessment, we describe the process followed to produce our dataset of destroyed buildings footprints (section 5.1.1). Visual analysis was performed using VHR optical images before and after event, as well as ancillary information such as OSM footprints and Google street view. We obtained a total of 375 buildings footprints classified as 'Destroyed' with a 'High' level of confidence. We also randomly selected an equal number of 'Non-destroyed' buildings for each Area of Interest (AOI), in order to compare the analyses of both damaged and non-damaged surfaces. From those 750 footprints, a buffer of 20m is shaped around to take in account co-registration of Sentinel-1 images, possible offsets or double bounce effects in urban areas.

Those resulting footprint and buffer are the input for the following analyses, alongside our SAR image collections. Our SAR dataset consists of Sentinel-1A image collections, covering 4 orbits with 13 acquisition dates per collection (11 before event and 2 after) (section 5.1.2).

As a preliminary analysis, we extract the mean intensity over time from each building footprint, for each orbit and polarization (section 5.2). These temporal signatures allow to examine the change of intensity values after event compared to before. We measure the deviation of trend after event relatively to the variability ( $\sigma$ ) before the event with a z-score standardization.

Subsequently, we make use of an unsupervised multitemporal change detection method taking in account the statistical properties of speckled data and the multilooking process. We begin with explaining the theory behind the method: the omnibus likelihood ratio test statistic (section 5.0.1). We prove the method's ability to apply to our case by comparing, with the theoretical chi-square distribution, the results of the omnibus tests for both our building footprint dataset (Destroyed and Non-Destroyed), as well as the whole AOIs for reference as urban area. We do so for both the 10 first images of our collection and the 3 last, which are one before and two after the event, and for each single polarization channel (section 5.3.1).

Then, a sequence of omnibus tests is used to determine where and when a change has occurred in our time series (section 5.3.2). This produces temporal change maps of the most recent change, the first change, and the frequency of changes. We measure the disaster impact with counts related to our building datasets to obtain metrics. At last, we will compare these outputs at the building level with their corresponding temporal signatures across various parameters.

The overall methodological framework is described in the following schema Fig. 14.

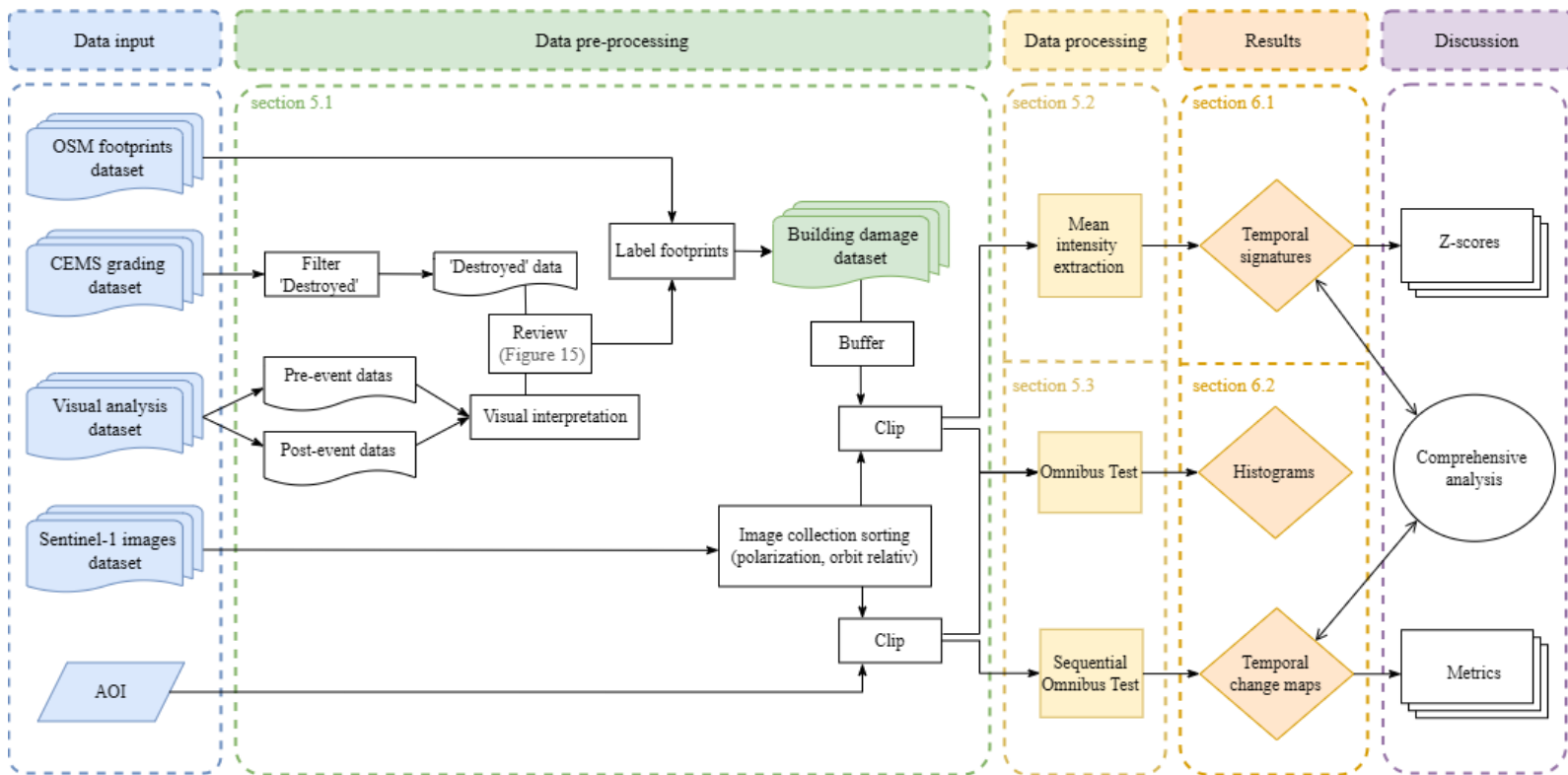


Figure 14: Overview of our methodological framework

### 5.0.1. Theoretical concepts

Our approach follows the omnibus likelihood ratio test statistic, which theory is explained below based on *the GEE tutorial* from Canty (2024). It results in temporal change maps that allow to represent the timeline of changes occurrence.

#### Hypothesis and Likelihood Functions

We formulate a null hypothesis, namely that no change has taken place in the signal strength  $a = |S_{vv}^a|^2$  between two images  $s_1$  and  $s_2$  acquired at times  $t_1$  and  $t_2$ , i.e.,

$$H_0 : \quad a_1 = a_2 = a$$

and test it against the alternative hypothesis that a change took place

$$H_1 : \quad a_1 \neq a_2.$$

If the null hypothesis is true, then the so-called likelihood  $L_0(a)$  for getting the measured pixel intensities  $s_1$  and  $s_2$  is defined as the product of the probability densities for that value of  $a$ . Under  $H_0$ , the *maximum likelihood* is obtained by maximizing  $L_0(a)$  with respect to  $a$  :

$$L_0(\hat{a}) = p(s_1|\hat{a})p(s_2|\hat{a}) = \frac{1}{\left(\frac{(s_1+s_2)}{2m}\right)^{2m}} \frac{(s_1s_2)^{m-1}e^{-2m}}{\Gamma(m)^2} \quad (5.1)$$

where  $\hat{a} = \arg \max_a L_0(a)$ .

Under the alternative hypothesis  $H_1$ , the maximum likelihood is:

$$L_1(\hat{a}_1, \hat{a}_2) = p(s_1|\hat{a}_1)p(s_2|\hat{a}_2) = \frac{m^{2m}}{\Gamma(m)^2} s_1 s_2 e^{-2m} \quad (5.2)$$

where  $\hat{a}_1, \hat{a}_2 = \arg \max_{a_1, a_2} L_1(a_1, a_2)$

#### A Likelihood Ratio Test

To minimize the probability  $\beta$  of an error of the second kind (  $H_0$  may be accepted when in fact it is false) for a fixed level of significance  $\alpha$ , we should reject the null hypothesis if the *ratio* of the two likelihoods satisfies the inequality:

$$Q = \frac{L_0(\hat{a})}{L_1(\hat{a}_1, \hat{a}_2)} \leq k \quad (5.3)$$

which is the Likelihood Ratio Test (LRT) for some appropriately small value of threshold  $k$ .

This definition simply reflects the fact that, if the null hypothesis is true, the maximum likelihood when  $a_1 = a_2$  should be close to the maximum likelihood without that restriction, given the

measurements  $s_1$  and  $s_2$ . Therefore, if the likelihood ratio is small, (less than or equal to some small value  $k$ ), then  $H_0$  should be rejected. In SAR change detection, the difference between two images is represented by their ratio, as ratio corresponds to subtracting logarithmic values for handling large ranges of SAR intensities. The quotients  $\frac{s_1}{s_2}$  and  $\frac{s_2}{s_1}$  are thus ratios of two chi-square distributed variables, each with  $2m$  degrees of freedom (cf Eq. 2.8 in chapter 2.2.1). This is corresponding to a F distribution, defined as the ratio of two chi square distributions, with  $m_1 = m_2 = 2m$  degrees of freedom. Therefore, for each pixel position in the two images, the quotient  $\langle s_1 \rangle / \langle s_2 \rangle$  is a LRT statistic as the F-distribution helps to define a decision threshold, whether or not a change has occurred between the two acquisition dates at that position.

In order to decide the test for  $Q_1 = s_1/s_2$ , we need the  $P$  value for a measurement  $q_1$  of the statistic.  $P$  value is the probability of getting a result at least as extreme as the one measured under the null hypothesis. So in this case

$$P_1 = \text{Prob}(Q_1 \leq q_1 \mid H_0), \quad (5.4)$$

which we can calculate from the percentiles of the  $F$  distribution. Then if  $P_1 \leq \alpha/2$  we reject  $H_0$  and conclude with significance  $\alpha/2$  that a change occurred. We do the same test for  $Q_2 = s_1/s_2$ , so that the combined significance is  $\alpha$ .

### The omnibus test

When comparing multiple images, a simple approach is to conduct pairwise comparisons. However, this approach makes it virtually impossible to control the rates of false positives (detecting a change where none exists) and false negatives (failing to detect an actual change). A more effective method for comparing several distributions is to perform a simultaneous test of the hypothesis of homogeneity across the distributions, commonly referred to as an omnibus test (Conradsen et al., 2016).

For the series of images acquired at times  $t_1, t_2, \dots, t_k$ , the null hypothesis is that, at a given pixel position, there has been no change in the signal strengths (i.e. amplitude)  $a_i = \langle |S_{vv}^a|^2 \rangle$  over the entire period, i.e.,

$$H_0 : a_1 = a_2 = \dots = a_k = a.$$

The alternative hypothesis is that there was at least one change (and possibly many) over the interval. This can be written succinctly as

$$H_1 : \exists i, j : a_i \neq a_j,$$

which says: there exist indices  $i, j$  for which  $a_i$  is not equal to  $a_j$ . Again, the likelihood functions

are products of gamma distributions:

$$L_1(a_1, \dots, a_k) = \prod_{i=1}^k p(s_i | a_i) = \frac{1}{\Gamma(m)^k} \left[ \prod_i \left( \frac{a_i}{m} \right) \right]^{-m} \left[ \prod_i s_i \right]^{m-1} \exp \left( -m \sum_i \frac{s_i}{a_i} \right) \quad (5.5)$$

$$L_0(a) = \prod_{i=1}^k p(s_i | a) = \frac{1}{\Gamma(m)^k} \left[ \frac{a}{m} \right]^{-mk} \left[ \prod_i s_i \right]^{m-1} \exp \left( -\frac{m}{a} \sum_i s_i \right) \quad (5.6)$$

and  $L_1$  is maximized for  $\hat{a}_i = s_i$ ,  $i = 1, \dots, k$ , while  $L_0$  is maximized for  $\hat{a} = \frac{1}{k} \sum_i s_i$ . After simplification our likelihood ratio test statistic is

$$Q_k = \frac{L_0(\hat{a})}{L_1(\hat{a}_1, \dots, \hat{a}_k)} = \left[ k^k \frac{\prod_i s_i}{(\sum_i s_i)^k} \right]^m \quad (5.7)$$

and is called an omnibus test statistic.

We can't expect to find an analytical expression for the probability distribution of this test statistic, so we will use Wilks' Theorem that states: under the null hypothesis  $H_0$  the statistic  $-2 \log Q_k$  follows a chi-square distribution as the sample size grows large. The degrees of freedom of this distribution are equal to the difference in the number of parameters estimated under the alternative and null hypotheses. Then,

$$-2 \log Q_k = \left[ k \log k + \sum_i \log s_i - k \log \sum_i s_i \right] (-2m) \quad (5.8)$$

should be approximately chi square distributed with  $k-1$  degrees of freedom under  $H_0$ . It allows us to determine p-values for hypothesis testing without needing to know the exact distribution of the test statistic  $Q_k$  under every possible scenario.

### The Sequential Omnibus Test

From Eq. 5.7, replacing the single polarization signal  $s_i$  by  $|c_i|$  the determinant of the polarimetric covariance matrix  $c_i$ ,  $\sum s_i \rightarrow \sum |c_i|$  and  $k^k \rightarrow k^{pk}$ , we get the general omnibus test statistic:

$$Q_k = \left[ k^{2k} \frac{\prod_i |c_i|}{|\sum_i c_i|^k} \right]^m \quad (5.9)$$

for the dual polarization image time series.

Decomposing Eq. 5.9 into a product of independent likelihood ratio tests will enable us to determine when changes occurred at each pixel location. For a series of length  $k$ , the omnibus test statistic  $Q_k$  may be factored into the product of likelihood ratio test's  $R_j$  which test for homogeneity in the measured reflectance signal up to and including time  $t_j$ , assuming homogeneity

up to time  $t_{j-1}$ :

$$Q_k = \prod_{j=2}^k R_j, \quad R_j = \left[ \frac{j^{2j}}{(j-1)^{2(j-1)}} \frac{|c_1 + \dots + c_{j-1}|^{j-1} |c_j|}{|c_1 + \dots + c_j|^j} \right]^m, \quad j = 2 \dots k. \quad (5.10)$$

Again we use Wilks' Theorem to get the P values, and work with:

$$-2 \log R_j = -2m \left[ 2(j \log j - (j-1) \log(j-1) + (j-1) \log \left| \sum_{i=1}^{j-1} c_i \right| + \log |c_j| - j \log \left| \sum_{i=1}^j c_i \right| \right] \quad (5.11)$$

and

$$-2 \log Q_k = \sum_{j=2}^k -2 \log R_j. \quad (5.12)$$

The statistic  $-2 \log R_j$  and  $-2 \log Q_k$  are approximately chi square distributed with 2 degrees of freedom and  $2(k-1)$  respectively.

To achieve this, we decompose Eq. 5.9 into a product of independent likelihood ratio tests, enabling us to determine when changes occurred at each pixel location.

### The sequential omnibus change detection algorithm

With a time series of  $k$  SAR images  $(c_1, c_2, \dots, c_k)$ ,

1. Set  $\ell = k$ .
2. Set  $s = (c_{k-\ell+1}, \dots, c_k)$ .
3. Perform the omnibus test  $Q_\ell$  for any changes over  $s$ .
4. If no significant changes are found, stop.
5. Successively test series  $s$  with  $R_2, R_3, \dots$  until the first significant change is met for  $R_j$ .
6. Set  $\ell = k - j + 1$  and go to 2.

The index  $\ell$  denotes the length of sequence  $s$  of images, starting with the  $\ell$ th image and ending with the last image  $c_k$ . The algorithm begins with the full sequence of images from  $c_1$  to  $c_k$ , and performs the omnibus test on the entire sequence simultaneously.

- **If no significant change is detected:** the process stops as the sequence is considered homogeneous.
- **If change is found in the sequence,** the series is truncated up to the point of change  $j$ : The algorithm proceeds  $R_j$  tests, starting with the smallest segment and progressively testing larger segments of the sequence  $s$  to find the first significant change at  $j$  (e.g.,  $R_2$  tests  $(c_1, c_2)$ ,

$R_3$  tests ( $c_1, c_2, c_3$ ), and so on until the change is found). Then,  $\ell$  is updated to  $k - j + 1$  which defines the length of the new subsequence that will be tested in the next iteration. There,  $Q_\ell$  test the remaining part of the sub-sequence (from  $c_{j+1}$  up to  $c_k$ ). If no change is found,  $j$  will be the first interval. If change is found, Step 5 and 6 keep over.

First, the entire sequence is tested; if no change is found, the sequence is considered homogeneous, and the process stops. If a change is detected, the series is truncated at the change point  $j$ , and smaller subsets are tested sequentially until the first significant change is identified. The process then continues with the remaining subsequence, building up thematic change maps:

- **cmap**: the interval of the most recent change, one band, byte values  $\in [0, k - 1]$ ,
- **smap**: the interval of the first change, one band, byte values  $\in [0, k - 1]$ ,
- **fmap**: the number of changes, one band, byte values  $\in [0, k - 1]$ ,
- **bmap**: the changes in each interval,  $k - 1$  bands, byte values  $\in [0, 1]$ .

Now, we will develop the method for our case. The implementation is detailed in Appendix A.

## 5.1. Data pre-processing

### 5.1.1. Production of a building footprint dataset

#### Introduction of CEMS damage grading

CEMS service of Rapid Mapping released a damage building assessment (EMSR648 for EAFZ event). They provide a standardized grading product in a vector package composed of the AOI, the imagery metadata, crisis information and shapefiles of damage assessments. Depending on the AOI, the grading product were generated by photo-interpretation or semi-automatic extraction, as describe in the marginalia of ready-to-use maps (Fig. 31 in Appendix). Beside this information and some definitions from the 'Online Manual' linked, the method used is rather opaque and unintelligible (Fig. 32 in Appendix).

The scaling categories used by CEMS for damage assessment of building structures are 'No visible damage', 'Possibly Damage', 'Damaged' and 'Destroyed'. This classification was inspired from the master's thesis and work of Cotrufo et al. (2018) on developing a building damage scale tailored for VHR vertical imagery analysis. We will only make use of the class 'Destroyed', as research indicates that lower damage classes cannot be detected with satellite remote sensing (Cotrufo et al., 2018).

### Review of CEMS damage grading

Out of 20 AOI for EMSR648 (Fig. 34 in Appendix), our dataset is built with AOIs 01, 02, 04 and 05. These cover the cities of Gaziantep, Adiyaman, Kahramanmaraş and Malatya respectively, gathering a total of 2.2 million people and 429 buildings labeled 'Destroyed', depending on the product chosen. Trying to build our dataset in a systematic way, we faced several error cases that are presented below with some examples.

A first inconsistency was identified in the occurrence of errors between the [MONIT] and [PRODUCT] packages (defined Fig. 33 in Appendix). For AOI01, the [MONIT] package included more 'Destroyed' buildings but also a significantly higher error rate compared to [PRODUCT] (Table 2). But for next AOIs, this pattern did not persist. To minimize errors, we selected the vector package with the fewest labeled buildings for each AOI. Table 1 lists the selected vector packages, and this selection results in a higher amount of correct classifications (Table 3). A second issue relates to feature representation: AOI01 was classified using points, while the remaining AOIs were represented by building blocks. Since our analysis focuses on the building level, we reassigned grading information by labeling OSM building footprints. Table 1 summarizes the reviewed products and the optical images used for each AOI. Figure 15 illustrates our visual analysis process.

	Source	Areas Of Interest			
		01	02	04	05
Building damages	CEMS	EMSR648 AOI01 GRA PRODUCT01 builtUpP_r1_v1_2	EMSR648 AOI02 GRA MONIT01 builtUpA r1 v1	EMSR648 AOI04 GRA MONIT01 builtUpP_r1_v1_3	EMSR648 AOI05 GRA PRODUCT builtUpA r1 v1
Pre-event	Sentinel-2 10 m	S2B_MSIL2A 25/01/2023	S2A_MSIL2A 27/01/2023	S2B_MSIL2A 25/01/2023	S2A_MSIL2A 20230127
Post-event	Google street view				
	Pleiades 50cm	11/02/2023	09/02/2023		09/02/2023
Post-event	WorldView02 30 cm	08/02/2023	08/02/2023	08/02/23	10/02/23
		12/02/2023	28/02/2023	12/02/23	
				28/02/23	
	UAV			Help.NGO UAV - Ebee - 09/02/2023	

Table 1: Summary of products reviewed and data used for visual interpretation and labels refinement

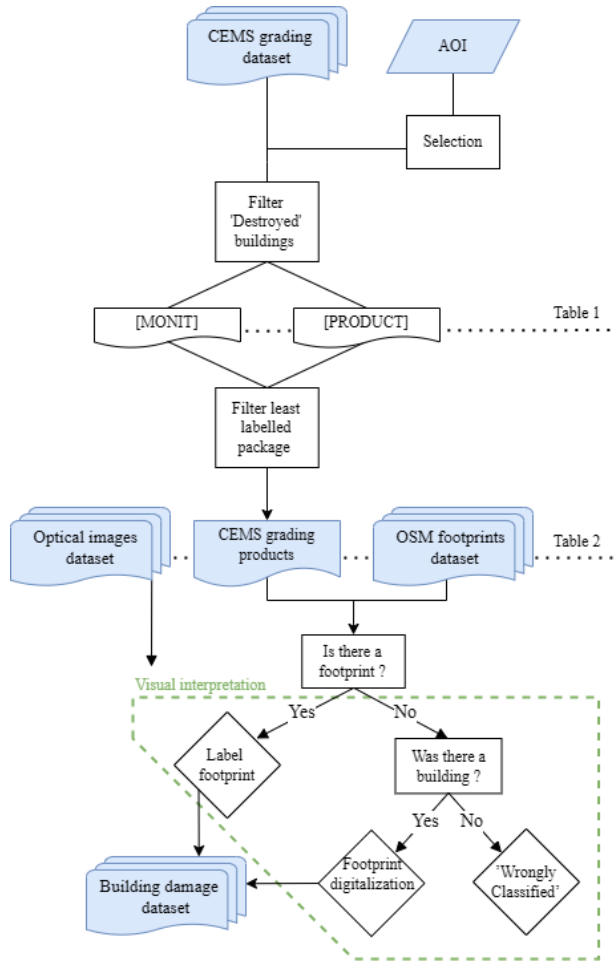


Figure 15: Schema of the visual analysis process

		AOI01	
		PRODUCT	MONIT
Grading scale		PRODUCT	MONIT
Built-up affected	'Possibly damaged'	13	19
	'Damaged'	4	9
	'Destroyed'	9	44
	<b>Total</b>	<b>26</b>	<b>72</b>
	Misclassified	20	39
	Correctly classified	6	33

Table 2: Summary of CEMS grading products for AOI01

### Visual Interpretation

**Errors in labelling target** We observed a pattern of redundant errors, where labels were assigned to non-buildings 16. It is often from an empty lot, debris, clutter or work site, that could visually look like a destroyed buildings or show a similar radiometric signature (*case 1*). Very likely, such errors come from a semi-automatic approach but it is lacking information on the method used. Visual analysis would recognize no building in pre-event image. This highlights the need to use ancillary information as mentioned in Chapter III.

We used the OSM Building footprint layer as pre- and post-event information (respectively released in 01/2023 and 11/2023). The comparison of OSM footprints at two different dates provides an initial information about the disappearance of a building. In many cases the label 'Destroyed' was given to places with no OSM building before event. The use of such dataset, open-source and frequently up-to-date, could avoid errors in further work. Another (*case 2*) was found labelling historical site and heritage ruins, despite the presence of OSM information. There are cases where the classified building was offset from the position of the actual disaster (*case 3*). For emergency services, this error is not significant as they would still locate the disaster, but it becomes an issue for an analysis that relies on building footprints. Sometimes, several labelled points were produced at one disaster location (*case 4*).

**Pre-event information handling** The downside of collaborative mapping is the non-exhaustive nature of the data. There may be missing information depending on the area. Typically, all of our AOIs were not fully mapped on the pre-event OSM layer. Interestingly, noticeable coverage progress was made on the post-event layer, due to works related to the event. In cases where the footprint was already lacking in the pre-event OSM layer, we used Google Street View, Sentinel-2 images and ancillary informations to evaluate if there has ever been a building (*case 1 : no*) (*case 6 : yes*). In this case, we digitize a building footprint.

By reviewing, we classified each point with three new attributes :

- 'MY\_Class' reviews the assessment from CEMS into 1 == 'Wrongly Classified' or 0 == 'Rightly Classified'
- 'NEW\_Class' assign 1 to all the buildings reviewed as 'Destroyed'
- 'LoC'  $\in [1, 3]$  assign a level of confidence from '1 == Certain' to '3 == Uncertain'

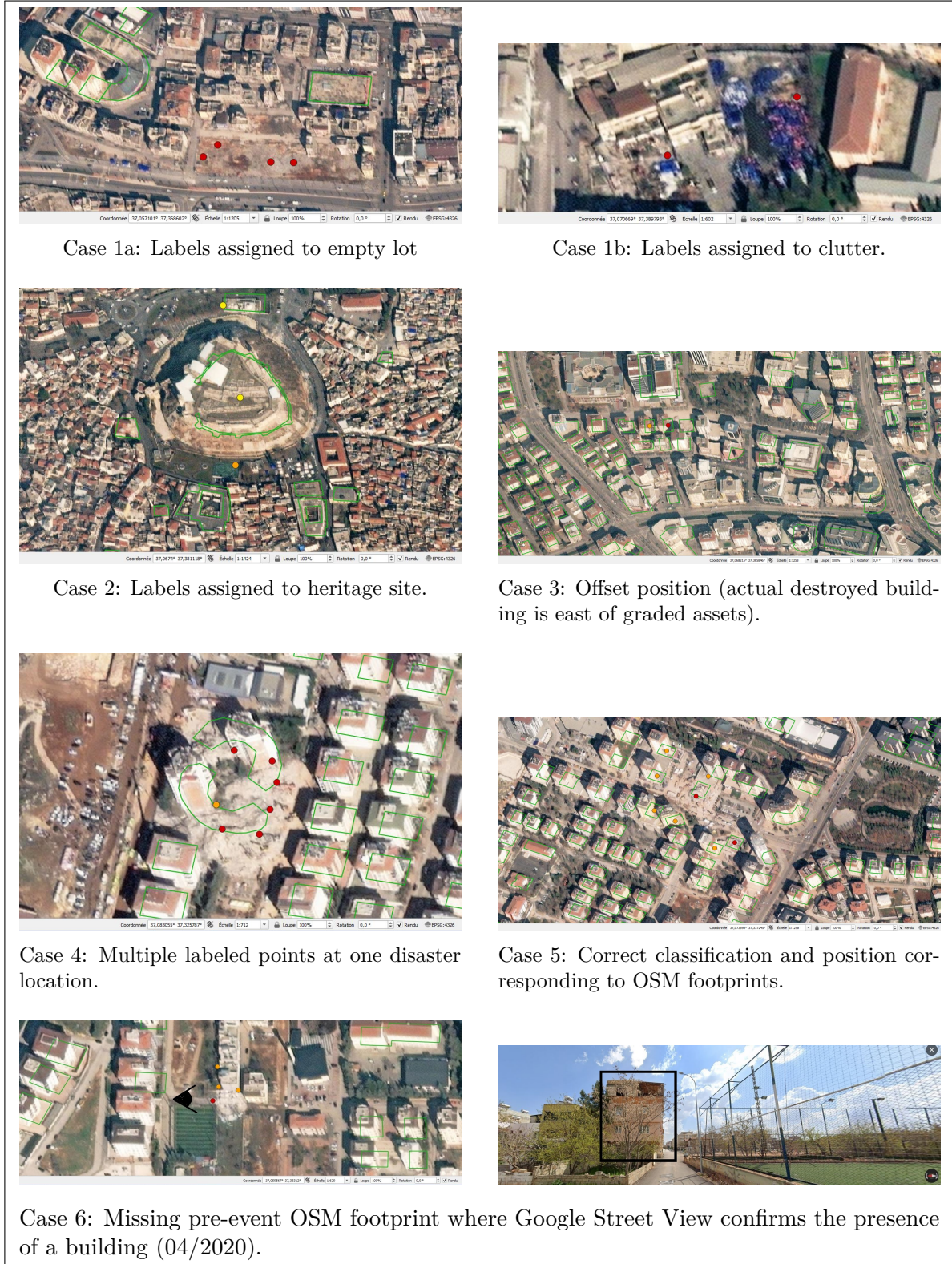


Figure 16: Overview of *Cases* encountered during review of CEMS products.

Pre-event OSM footprints (green polygons) and CEMS graded assets (points; Red: 'Destroyed', Orange: 'Damaged', Yellow: 'Slightly damaged').

The background is the WorldView02 post-event image from 12/02/2023.



Case 7 : Missing and unlabelled footprints (blue polygons). Misclassified points (blue) are in fact street parking. Correctly classified points (green). Foreground : Help.NGO UAV image

		Areas Of Interest				Total
		01	02	04	05	
Estimated population (x1000 hab)	01	1191	210	385	423	2209
	'Destroyed'	9	32	286	102	429
	Misclassified	3	1	16	13	34
	Correctly classified	6	31	270	89	395
	Missing		7	29	3	39

Table 3: Summary of CEMS grading products for each AOI

The results of our classification are presented in Table 3 above. The grading products for these areas contain 429 buildings or blocks classified as 'Destroyed'. I labelled 395 as 'Correctly classified', with 356 of these assigned with 'High' level of confidence. To build our reliable dataset of buildings, we selected only those assigned with 'High' level of confidence. Additionally, 39 unaccounted buildings that had actually been destroyed were identified, particularly with the help of VHR images acquired from UAV at AOI04 (*case 7*). We merged these 39 with our selection of CEMS reviewed buildings, resulting in a total of 375 buildings classified as 'Destroyed'. We also randomly selected an equal number of non-damaged buildings for each AOI, in order to compare the analyses of both damaged and non-damaged footprints. From those 750, a buffer of 20m is shaped around to take in account co-registration of S-1 images, possible offsets or double bounce effects in urban areas. These resulting footprints and buffers will be the input (OSM\_batch1, OSM\_buffer) of our change detection model using SAR imagery.

### 5.1.2. Sentinel-1 Images Dataset

The SAR images dataset was collected from Copernicus Sentinel-1 Ground Range Detected. It is essential that the local incidence angles be the same in each images collection, for which we specify both the orbit pass and the relative orbit number. Their coverage can be found through the Copernicus Acquisition Plan Viewer. Our study area is covered by 4 orbits: Descending (DESC) **21** and **123** as well as Ascending (ASC) **14** and **116**. With the disaster event dated 06/02/2023, and with Ascending and Descending pass shifted 6 days from each other, our image collections spans from 01/10/2022 to 02/03/2023 for DESC, and 01/10/2022 to 13/03/23 for ASC. We note an 11-day difference between the two image collections, as the GEE image collection for orbit 116 is lacking one date between 04/02/23 and 28/02/23. Then, we have a total of 13 acquisition dates per collection with 11 before event and 2 after. Their imprints are displayed for each orbit in Fig. 17.

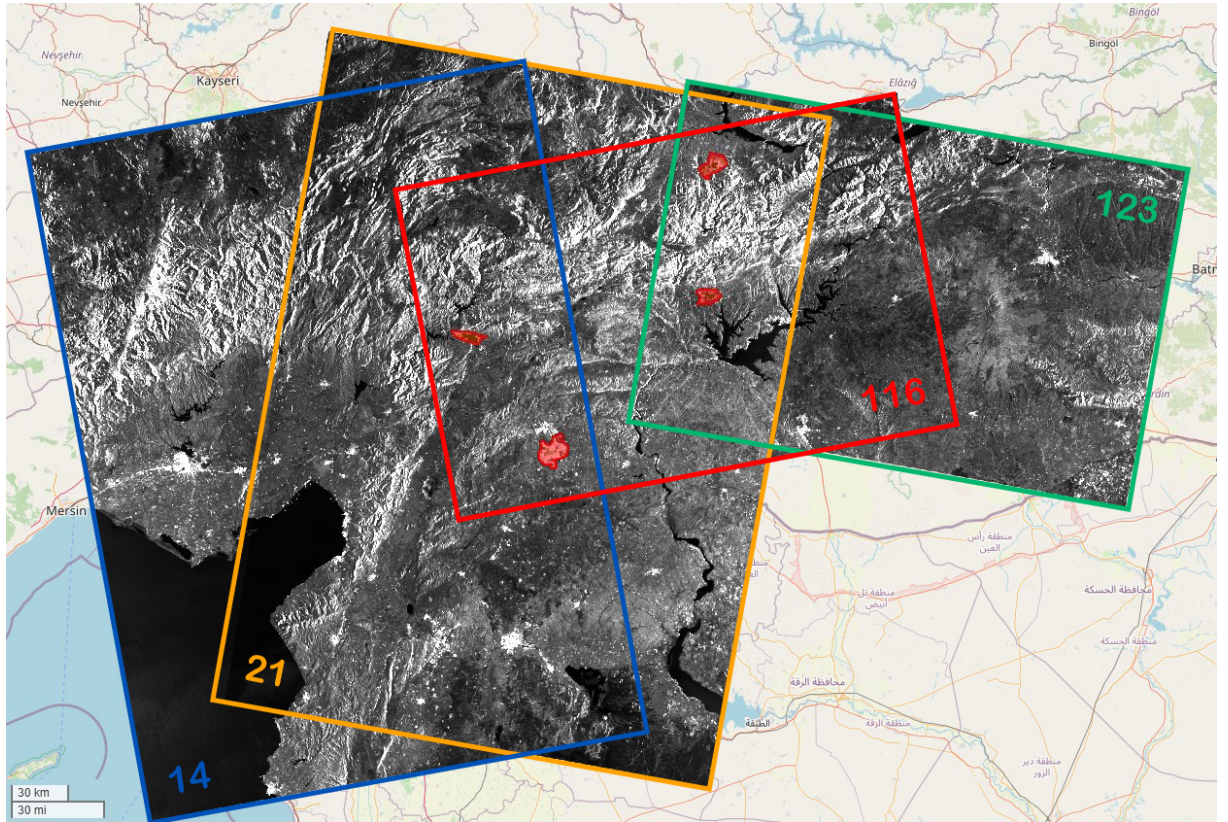


Figure 17: Sentinel-1 Images Collections Imprints covering our AOIs (red)

## 5.2. Intensity temporal signatures of Destroyed building

As a first analysis, this section studies the backscattered intensity of our image collection over time from each building footprint. We built a program for extracting, processing, and visualizing time series intensity for building footprints in an interactive chart. This allows to visualize and examine the trend of each building signature before/after event, for each orbit relative and polarization. Our implementation is described in Appendix A.

Each of the 375 Destroyed building, is covered by three relative orbit with two polarizations available, for a total of 2250 signatures. Over our timeframe of 13 dates, it will give a total of 29 250 values: the mean intensity over the footprint geometry at instant  $t$ . This dataframe will be the input for the interactive charts described below.

We obtain the final tool of this section 5.2, an interactive chart displaying the mean intensity for each building footprint over time, with distinct polarization types and relative orbits. We programmed a different option to observe only one relative orbit for example. The Observable HQ Notebook will be more suitable for data visualization and such options filtering.

To measure deviations in building signatures after the event compared to before, we perform a z-score standardization:

$$z = \frac{\text{mean}_{\text{after}} - \text{mean}_{\text{before}}}{\sigma_{\text{before}}}$$

Over our 2250 signatures, we expressed the percentage of signatures inside a range of z-scores in Table 4. We ran the model on both 20-m buffer and no-buffer footprints datasets.

The results are presented section 6.1 and show complementary responses between orbits and channels, if one fails to detect a change, the other succeeds. Therefore, it would be beneficial to exploit both channels, which is precisely the purpose of the covariance matrix. The sequential omnibus test uses the determinant of the covariance matrix to compute a test statistic assessing the overall differences between distributions at multiple times. This method also takes in account the statistical properties of speckled data and the multilooking process.

## 5.3. Multitemporal change detection

### 5.3.1. The omnibus test statistic

To prove Wilk's theorem and the method's ability to apply to our case using , we compare the results of omnibus tests with the theoretical chi-square distribution performed simultaneously for all 10 first images, for the 3 last -one before and two after the event- and for all the pixels of both building footprint dataset (Destroyed and Non-Destroyed) as well as the whole AOIs for reference as urban area. To compare, we did so for each single polarization channel. We obtain the histograms of frequency of values resulting from the omnibus test for each pixel of the mentioned dataset (Fig. 20 in chapter Results 6.2.1).

It allows us to control the overall false positive probability  $\alpha$ , so we can generate a change map for the entire time series. However, this map does not provide any information about the temporality of the changes and is therefore not addressed in this paper.

### 5.3.2. The sequential omnibus change detection

Instead of testing the entire time series simultaneously, the sequential omnibus change detection algorithm divides the timeline into sequences and detects changes iteratively to build up the change pattern for all pixels over all time points. We run the algorithm, for Orbit 116 ASC, then for Orbit 21 DESC, for the different levels of significance. We obtain temporal change maps of the most recent change `cmap`, the first change `smap`, the frequency of changes `fmap` and the changes in each interval `bmap` that we can clip (or not) to our buildings footprints. There, we can detect at which interval and at which frequency changes occurred, opening plenty of possibilities depending on the needs.

The disaster event happened at interval n°11 of our sequences of images. To see the changes occurring at this interval, we isolate the bitemporal map (`bmap`), which displays the changes detected between the image before and after (Fig. 35). We relate the situation to give an idea on a 'usual day' before event, selecting interval 10 for example (Fig. 36).

Those maps give spatial information that we complete with statistics: first, we counted the frequency of values (1=change detected or 0= change not detected) taken by each pixel inside all footprints of both datasets, using different '`Scale`' parameter. Then, to count the number of buildings considered as 'Destroyed', we measured the sum of 'change' pixels inside each building polygon and filter buildings with values greater than 0 to obtain a count of buildings having change within their footprint. The results are displayed in Table 5. Finally, with the count of buildings impacted or not during event, we can measure metrics to evaluate the performance of this approach for the different levels of significance.

We do the exact same process for the start map (`smap`), which identifies pixels where a change occurred for the first time at interval  $t$ , without detecting any changes in previous intervals. This approach would avoid catching pixels prone to frequent changes. Ultimately, this allows to compare the performance of the bitemporal and the multitemporal approach with start map

## 6. Results

### 6.1. Intensity temporal signatures of Destroyed building

The output of section 5.2 results in the intensity temporal signatures of Destroyed building for each orbit and polarization. Here is a glimpse for a sample of 2 signatures. The Observable HQ Notebook is more suitable for interactive data visualization and options filtering.

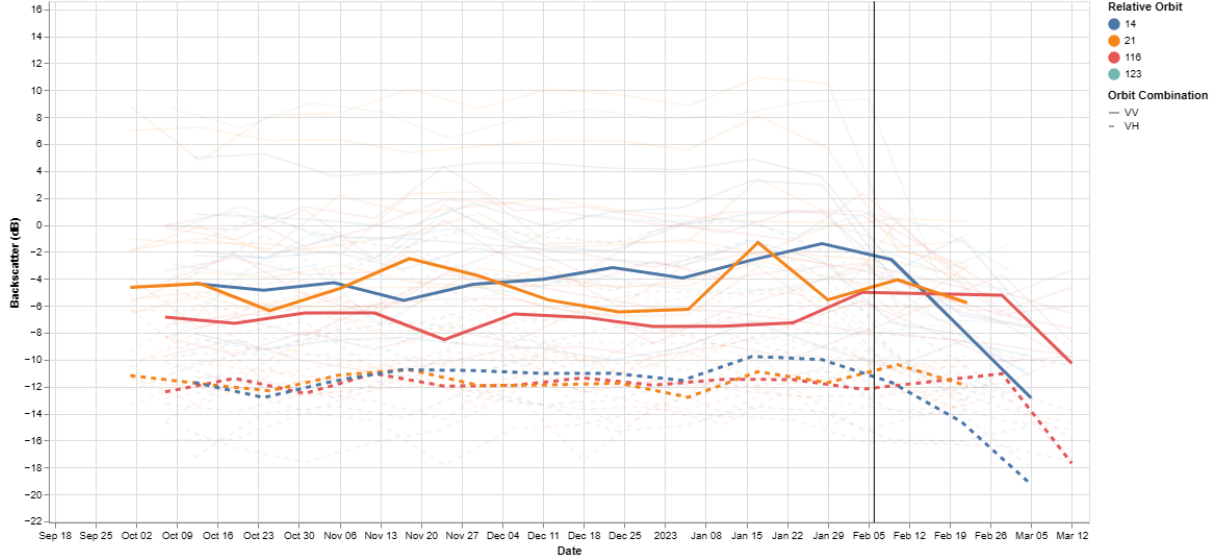


Figure 18: Intensity (dB) temporal signature for footprint ID 352308002 by polarization and relative orbit.



Figure 19: Intensity (dB) temporal signature for footprint ID 222765255 by polarization and relative orbit.

The mean intensity for the footprint Figures 18 and 19 show a clear slope break for most channels and orbits after the event, confirming the ability to detect a change of trend in intensity return from a building footprint after its destruction. The chart also highlights several key points:

- For a same building, change is more apparent with certain orbits (Fig. 18 orbit 21 (orange) displays no significant change of trend unlike the other orbits).
- Intensity can also increase after the event, for one polarization but not the other; (Fig. 19 orbit 116 (red)).
- Overall, we observe a complementary response between orbits, as well as channels, where if one failed to detect a change, the other succeeded. This observation will drive our analysis forward.

From these signatures, the z-scores indicates the extent of deviation after event compared to before. Hence, most buildings signatures show deviation: 371 have at least one signature outside  $+/- 1\sigma$  z-scores, which sets a thresholds for indicating change.

Threshold	Range (%)			Threshold	Range (%)		
	Below -	Between	Above +		Below -	Between	Above +
$1\sigma$	45	36	18	$1\sigma$	50	35	15
$2\sigma$	28	61	9	$2\sigma$	33	60	7
$3\sigma$	17	76	5	$3\sigma$	20	75	5

(a) No buffer

(b) Buffer

Table 4: Range of z-scores for all signatures

The scores Table 4 for all signatures provide a first idea of the magnitude of deviations from intensities after event compared to the trend before. For example, the first cell shows that around 45% of our 2250 signatures got mean intensities after event below  $-1\sigma$  compared to the trend before. Out of the 2250 signatures, around 65% of them are outside  $+/- 1\sigma$  for both footprint datasets. With buffer, we capture more signatures with deviations below the threshold than without it and fewer that are above. This could be explained by the loss of double-bounce reflection toward the sensor. A buffer including surrounding pixels is more prone to this overall loss of double-bounce. Also, a significant amount of signatures (around 1/4) deviate from more than three standard deviation after event. There, the change of trend is outstanding.

To conclude, this preliminary analysis allows us to highlight a few key points. We confirmed the change of trend in intensity return from a building footprint after its destruction. The use of buffer around the footprint appears to be efficient in detecting changes of trend. Considering the complementary signatures between polarizations, it would be beneficial to exploit both channels, which is precisely the purpose of using the determinant of the covariance matrix to compute the test statistic assessing the overall differences between distributions at multiple times during the sequential omnibus test.

## 6.2. Multitemporal change detection

### 6.2.1. The omnibus test statistic

The results of the omnibus tests performed for all pixels of both our building footprint dataset and the whole AOIs, simultaneously for entire sequences of images pre- and during event, are first compared with the theoretical chi-square distribution.

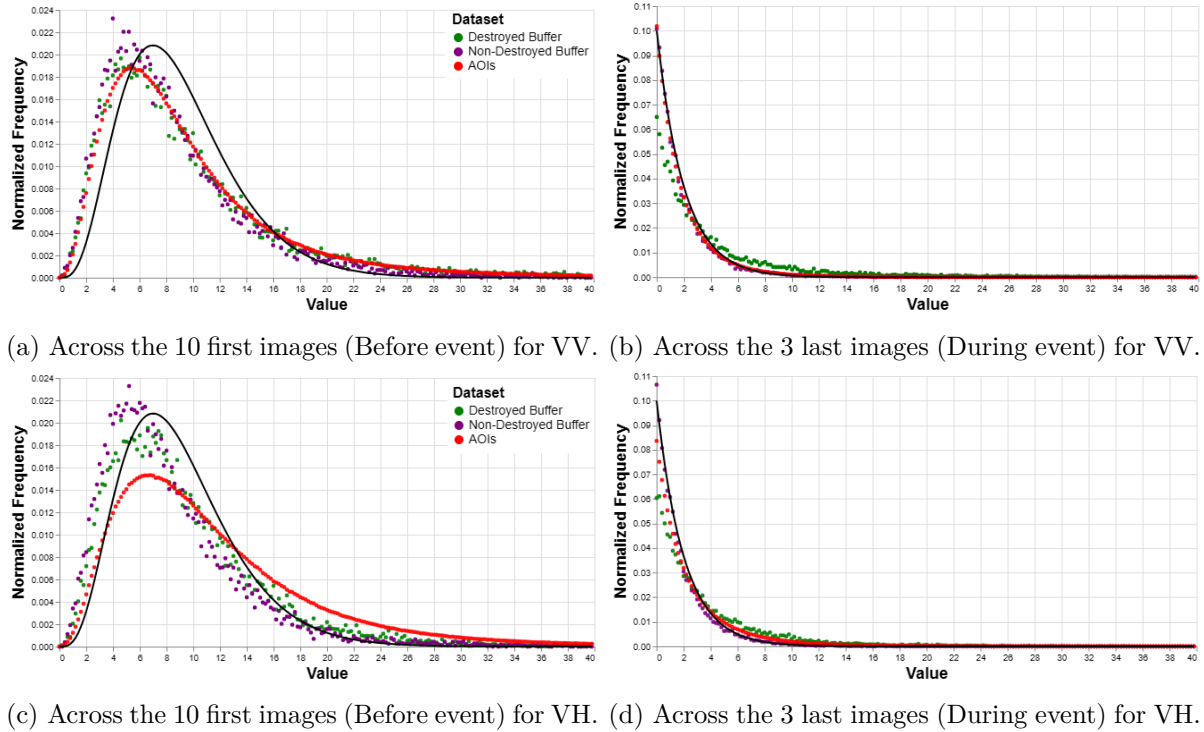


Figure 20: Histograms of values from omnibus tests performed simultaneously across the entire specified sequence of images performed over the whole AOIs and footprints datasets. (a) and (b) correspond to VV polarization, while (c) and (d) correspond to VH polarization. All datasets follow the theoretical chi-square distribution (black) which confirms Wilk's theorem. Higher frequency of changes are detected during event (c and d) for the 'Destroyed' dataset.

These histograms present the frequency of values obtained from the omnibus tests, conducted on the mentioned dataset simultaneously applied across the entire sequence of specified images. The method is proven to apply to our case as Wilk's theorem is a good approximation: before event (Fig. 20a), all datasets follow the theoretical chi-square distribution (black). During event (Fig. 20b), the 'Non-Destroyed' (purple) and AOIs (red) distributions also follow closely the chi-square distribution as expected for no change, while the 'Destroyed' dataset (green) present some deviation from the theoretical distribution. Relatively less frequent low values (lower than 4), which indicates less occurrences of no change, and more high values at the tail, which indicates higher frequency of changes: changes are effectively detected within the 'Destroyed' footprints for the sequence of images during event. Another interesting result is the distribution of values for VH channel (Fig. 20c) over all the AOIs pixel's displaying more changes than for VV. This is explained by cross-polarization being more sensitive to surface roughness and texture changes, particularly in heterogeneous environments such as urban areas.

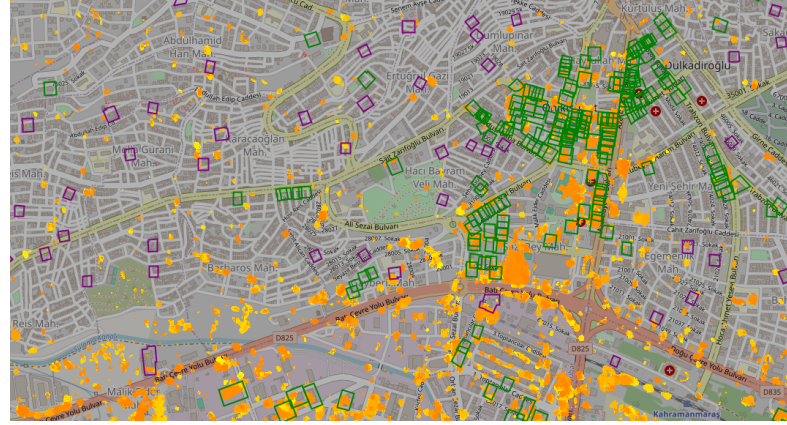
With the method proven to apply to our case, and change detected within the 'Destroyed' footprints during event, we can now use the test in a sequential way to determine where and when changes have occurred.

### 6.2.2. The sequential omnibus change detection

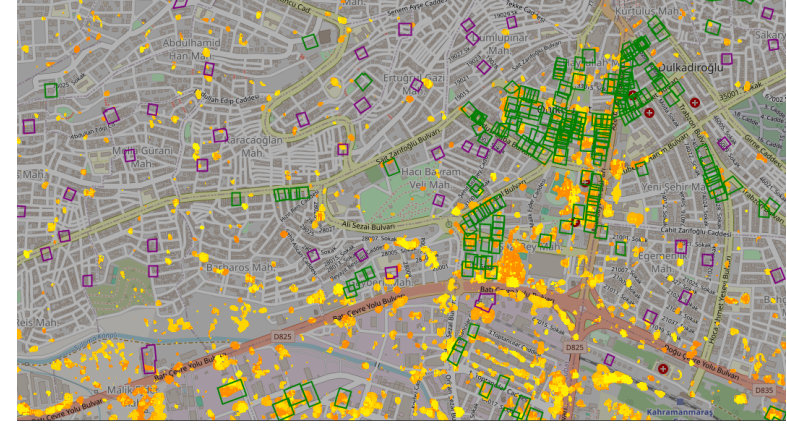
The sequential omnibus algorithm allows us to generate multitemporal change maps:

- **cmap**: the interval of the most recent change, Fig. 21a,
- **smap**: the interval of the first change, Fig. 21b,
- **fmap**: the number of changes, Fig. 21c,
- **bmap**: the changes in each interval, Fig. 35 to 38 in Appendix,

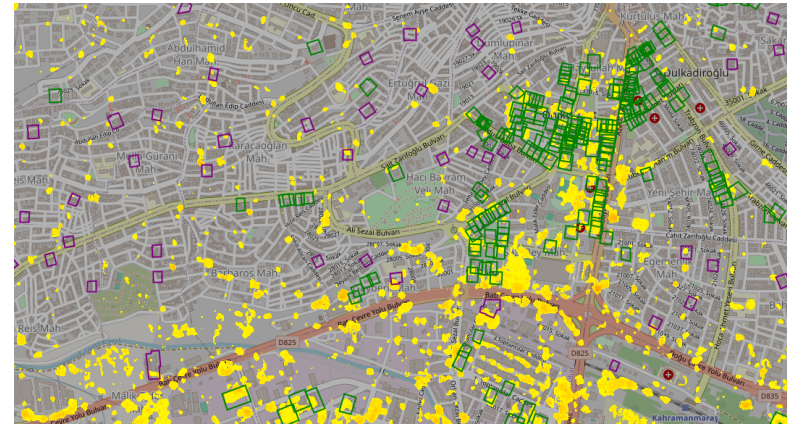
that we can clip with our building footprints to relate changes with the disaster, or not, to observe the situation at the city level. Then, we can detect at which interval changes occurred and at which frequency, opening plenty of possibilities depending on the needs.



(a) Change map (**cmap**): the interval of the most recent change (yellow: early, orange: late).



(b) Start map (**smap**): the interval of the first change (yellow: early, orange: late).



(c) Frequency map (**fmap**): the number of changes (yellow: few, orange: many).

Figure 21: Multitemporal change maps for Kahramanmaraş (AOI4).

Green: 'Destroyed' footprints; purple: 'Non-Destroyed' footprints.

Changes are detected corresponding with 'Destroyed' footprints, in contrast to other areas. The frequent changes in the south correspond to an industrial zone.

The temporal maps displayed Fig. 21 cover the whole time series and contain too much information for assessing damage related with the event, necessitating further analysis. In this regard, the following section will present different ways to explore these outputs focusing on the most relevant changes. We will compare change maps at interval before and during event alongside with statistics related to the buildings dataset.

### The bitemporal map

The bitemporal map (`bmap`) displays the changes detected at interval during event (Fig. 35 in Appendix between the image before and after event), or on a 'random interval' before event (Figure 36 in Appendix) to observe a 'usual situation'. The difference between the two maps is striking as more changes are detected during event compared to before.

The center of Kahramanmaraş (AOI4) was particularly impacted, which corresponds to many 'Destroyed' footprints. However, some changes were already occurring at the interval before event, such as the south of AOI4 which correspond to an industrial zone. Typically, roads and parking are also displaying recurrent changes. These spatial information are measured with counts related to the building datasets in Table 5.

Footprint Dataset	Scale=10				Scale=5			
	During event		Before event		During event		Before event	
	Destroyed	Non- Destroyed	Destroyed	Non- Destroyed	Destroyed	Non- Destroyed	Destroyed	Non- Destroyed
Values 0.0	13,756	14,404	14,575	14,399	53,207	57,286	57,905	57,398
Values 1.0	1,089	30	270	35	6,077	481	1,379	369
Buildings with changes	176	21	101	18	255	78	177	62

Table 5: Pixel values and count for bitemporal map `bmap` and count of buildings with changes detected within, at interval during event and before, for different `Scale`

First, we compare the amount of pixels with changes inside the 'Destroyed' footprints compared to those without changes:

- During event, we detected 1.089 pixels with changes out of 13.756 without, and 6077 out of 53207 without, for `Scale=10` and 5 respectively.
- Before event, both datasets have a relatively similar count of few pixels with changes (270/14575 and 35/14399 for `Scale=10`; 1379/57905 and 369/57398 for `Scale=5`). However, this does not reflect in terms of count of buildings as relatively 101 and 177 buildings contain changes within their footprint even before disaster.

We conclude that either this map or the way of considering a building as 'Destroyed' is overestimating disaster. Moreover, those results are much depending on the '`scale`' parameter in the '`reduceRegion`', that defines the size in meters of each pixel in the method.

Now with the count of buildings impacted or not during event, we can measure metrics to evaluate the performance of this approach. Using the count of footprints 'Non-Destroyed' as False Positive (FN) if change is detected within, the count of 'Destroyed' buildings will give the True Positive, and the difference with the total amount of 375 entities for each dataset will give the True Negative and False Negative rate:

- **True Positives (TP)**: buildings 'Destroyed' where a change is detected.
- **False Positives (FP)**: buildings 'Non-Destroyed' where a change is incorrectly detected.
- **True Negatives (TN)**: Total - FP : buildings 'Non-Destroyed' correctly identified.
- **False Negatives (FN)**: Total - TP : buildings 'Destroyed' that the model failed to detect change within.

The number of buildings classification (TP, FP, FN, TN) is summarized 11 in Appendix. The metrics formulas are defined Fig.39 also in Appendix and represent:

- **Precision** measures the amount of buildings correctly identified as 'Destroyed'. High precision means the model is reliable when it predicts a building as 'Destroyed.'
- **Recall** measures the model's ability to find buildings that were truly 'Destroyed.' A high recall indicates the model detects most of the actual destroyed buildings.
- **F1 score** is the harmonic mean of precision and recall. It balances these two metrics providing a single measure of performance.
- **Accuracy** reflects the proportion of total predictions that are correct, relatively to the entire datasets of 750 buildings.
- **Specificity** measures the ability to correctly identify 'Non-Destroyed' buildings. High specificity indicates the model is good at avoiding false alarms for 'Non-Destroyed' buildings.

	During event	
Metric	Scale = 10	Scale = 5
Precision	0.894	0.766
Recall	0.469	0.680
F1 Score	0.615	0.720
Accuracy	0.707	0.736
Specificity	0.944	0.792

Table 6: Metrics for bitemporal map **bmap** with different **scale**

The scale parameter has a significant impact on the amount of buildings classified as 'Destroyed' which defines the performance of the model. It is either lacking precision at a small scale or too conservative using a bigger scale of analysis. As Risk Management is particularly focus on allocating the emergency resources at the correct location, we shall try to lower the rate of False Positive, with high Specificity, while maintaining a high recall, meaning capturing correct classifications.

### **The start map**

To do so, we used the start map (**smap**), which identifies pixels where a change occurred for the first time at interval  $t$ , without detecting any changes in previous intervals. This approach would avoid catching pixels where changes already occurred. Clearly, the maps of the first changes (**smap**) display fewer changes compared to the previous bitemporal maps (**bmap**) at same intervals respectively. We observe few first occurrences of change at the interval before event (Fig. 38 in Appendix). In comparison, the interval covering the event shows significantly more first changes (Fig. 37 in Appendix). We can notice a correlation with the 'Destroyed' footprints, AOI4 for example, which we measure similarly as previously in the counts Table 7 and the metrics Table 8 :

	Scale = 10				Scale=5			
	During event		Before event		During event		Before event	
Footprint Dataset	Destroyed	Non-Destroyed	Destroyed	Non-Destroyed	Destroyed	Non-Destroyed	Destroyed	Non-Destroyed
Values 0.0	14,166	14,428	14,576	14,414	55,554	57,592	58,713	57,611
Values 1.0	680	6	100	20	3,729	175	571	157
Buildings with Changes	147	10	64	12	232	48	118	35

Table 7: Pixel values and count for start map **smap** and count of buildings with changes detected within, at interval during event and before, for different **Scale**

Looking at the amount of pixels inside footprints supposed to not detect changes (Non-Destroyed during event and both datasets before event), we did succeed in avoiding overestimation of changes. However, the amount of 'Buildings with changes' from the 'Destroyed' dataset before event remains very high. This indicates that the method of counting buildings is responsible for overestimating the number of buildings with changes unrelated to the event. This overestimation can likely be attributed to the spatial proximity of 'Destroyed' footprints and their buffer overlapping, counting several different buildings if change occurred where their buffer overlap. In contrast, 'Non-Destroyed' footprints are more randomly distributed and spread out.

Again, we measure metrics to evaluate the performance of this approach.

Metric	During event	
	Scale = 10	Scale = 5
Precision	0.936	0.829
Recall	0.392	0.618
F1 Score	0.554	0.707
Accuracy	0.683	0.745
Specificity	0.973	0.872

Table 8: Metrics for smap (**smap**) for different **scale**

Compared to the bitemporal **bmap**, the **smap** of first changes is better at correctly identifying non-destroyed buildings, as it filters pixels that didn't change until the event: it minimizes false positives, which leads to higher precision and specificity in both scales. However, it is less effective at identifying all destroyed buildings which results in a lower recall. The best compromise, as F1-score, does not outstand between each map, but do for the use of **scale=5**. Then, let's keep that scale for further analysis.

### Sensitivity analysis of both maps performances

Until now, the analysis was performed on Orbit 116 with level of significance  $\alpha$  set at 2,5%. We can evaluate the sensitivity of our model to by measuring the metrics at different levels of  $\alpha$ . And doing so for orbit 21 will give us an insight on the performance for each orbit :

	$\alpha$				$\alpha$		
	1%	2.5%	5%		1%	2.5%	5%
Precision	0.817	0.766	0.740	Precision	0.852	0.829	0.833
Recall	0.608	0.680	0.776	Recall	0.539	0.618	0.705
F1 Score	0.695	0.720	0.758	F1 Score	0.652	0.707	0.764
Accuracy	0.735	0.736	0.750	Accuracy	0.722	0.745	0.774
Specificity	0.864	0.792	0.728	Specificity	0.907	0.872	0.844

(a) bitemporal map (**bmap**)

(b) Start map (**smap**)

Table 9: Model Sensitivity Analysis of change maps for Orbit 116 with **scale=5**

	$\alpha$		
	1%	2.5%	5%
Precision	0.802	0.774	0.727
Recall	0.703	0.789	0.829
F1 Score	0.749	0.781	0.774
Accuracy	0.765	0.780	0.759
Specificity	0.827	0.770	0.688

	$\alpha$		
	1%	2.5%	5%
Precision	0.873	0.842	0.823
Recall	0.659	0.728	0.741
F1 Score	0.750	0.781	0.780
Accuracy	0.785	0.799	0.789
Specificity	0.905	0.865	0.840

(a) bitemporal map (**bmap**)(b) Start map (**smap**)Table 10: Model Sensitivity Analysis of change maps for Orbit 21 with **scale=5**

For both orbits, as alpha increases, the precision tends to decrease, while the recall increases. This is consistent with the general trade-off between precision and recall, catching more TP allow more FP. The **smap** (b) of first change generally shows higher precision and specificity but lower recall compared to bitemporal map **bmap** (a). It minimizes FP but misses some TP cases. As mentionned above, avoiding pixels where changes already occurred leads to filter both cases. Comparing orbits, F1-score and accuracy are higher for Orbit 21 (Table 10) than for Orbit 116 (Table 9) thanks to the better recall. Though, this not the case for specificity, which we focus for risk assessment, having both similar performance.

To sum up, in this section we evaluated the performance of the model for both bitemporal **bmap** and **smap** of first change. Both show consistent performance with slight deviation across different levels of significance. Depending on the priority of risk assessment, being missing true cases or avoiding FP, the map of first change, avoiding pixels where changes occurred, is more interesting with its high specificity. However, those metrics are very relying on the scale parameter which determines the amount of buildings classified as 'Destroyed'. After addressing overestimation using the **smap** of first changes, we also conclude that the method of counting buildings is responsible for overestimating the number of buildings with changes unrelated to the event. More discussion is presented in the next chapter.

---

## 7. Discussion

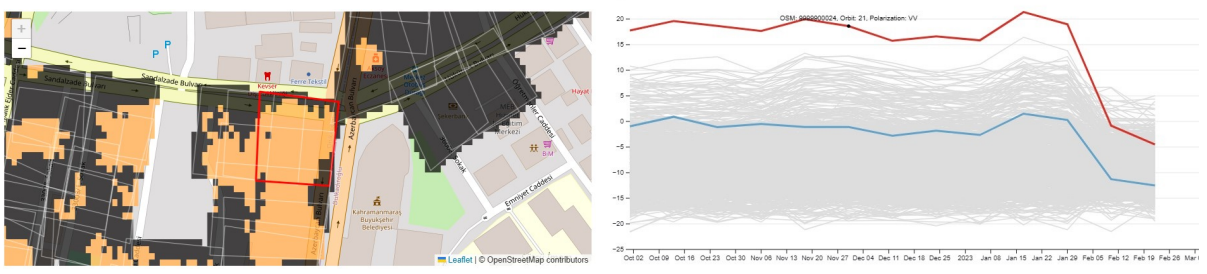
In this chapter, we first explore the results of both analysis at the building level and reflect on them in regard to the research objective. Then, we review the performance of our model compared to the studies on the East Anatolia event mentioned chapter 3. Finally, we present some limits of this study, opening perspectives for further work.

The results of temporal signatures (section 6.1) gave more contrast between both orbits. It is worth examining beyond metrics, at the building level, the conditions under which the output of both analysis can complement each other in providing insights about the model. Toward this end, the interactive tool developed using ObservableHQ enables to examine the temporal signatures and mapped change occurrences across various parameters, offering a complementary perspective for understanding. Before all, let's remind Ascending pass (116) is sending signal eastward and Descending pass (21) is westward.

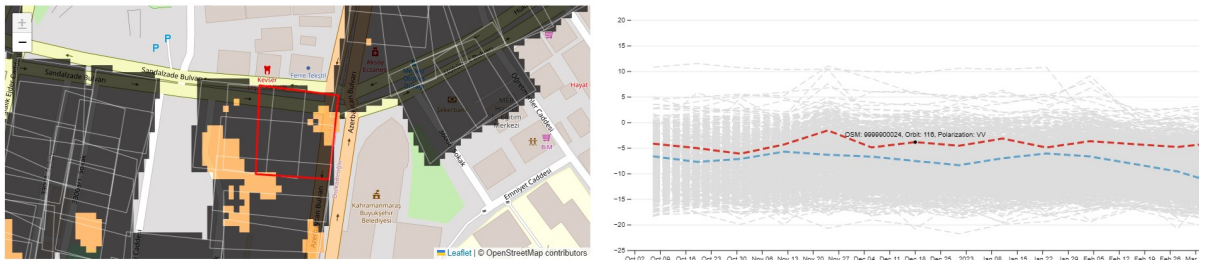
### Complementary orbits

Let's start with the temporal signature showing the highest mean trend and a significant drop in intensity: building with OSM ID 9999900024, having a z-scores around -12 and -8 for orbit 21 (Fig. 22a) and of 0 and -5 for orbit 116 for VV and VH respectively (Fig.22b). This case is a good example of agreement between the temporal signatures and the change map: the signature from orbit 21 is ruptured and detected change while not from orbit 116. The building's position at the intersection of streets to the east may explain the strong signal from the Descending sensor on that side. In contrast, detection by orbit 116 on the west side could be affected by shadowing from the neighboring building.

The entire street also seems more responsive to the east-facing orbit 21 (Fig. 22d) than to orbit 116 (Fig. 22c). On the west-side of building block (circles in green), some buildings facing the orbit 116 sensor did catch a change, with z-scores of -2 (VV) and -5.9 (VH) for OSM ID 472863214.



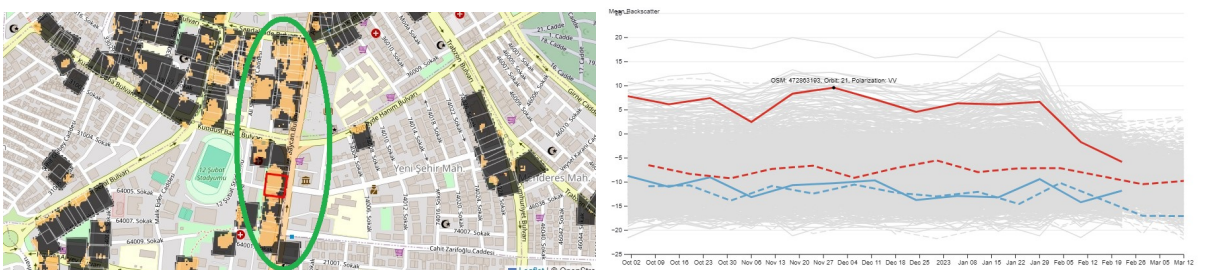
(a) Smap Orbit 21: shows change detection, consistent with the temporal signature - OSM ID 999900024.



(b) Smap Orbit 116: shows no change detection, consistent with the temporal signature - OSM ID 999900024



(c) Smap Orbit 116: East-oriented buildings (circled in green) indicate changes toward the sensor. The temporal signature drops significantly for Orbit 116 but not for Orbit 21 - OSM ID 472863214.

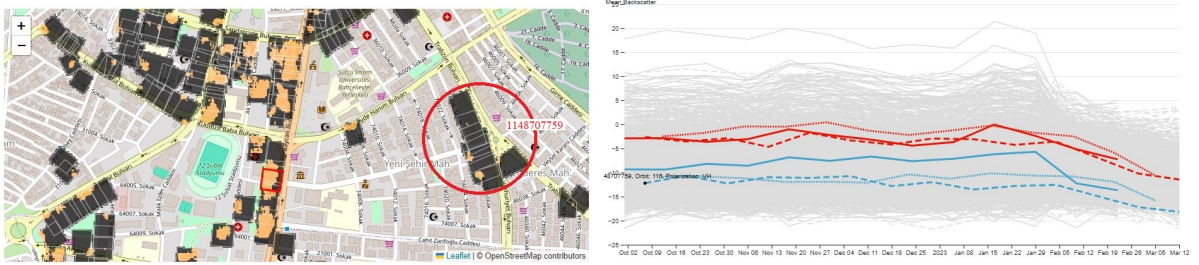


(d) Smap Orbit 21: West-oriented buildings (circled in green) indicate changes toward the sensor. The temporal signature drops significantly for Orbit 21 but not 116 - OSM ID 472863193

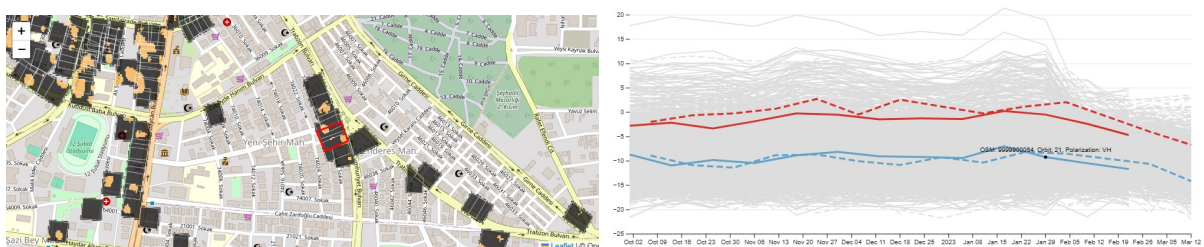
Figure 22: Comparison of temporal signatures and start map (**smap**) of first change for various footprints. Temporal signatures: Orbit 21: full line; Orbit 116: dashed line; VV: red; VH: blue.

### Undetected damage for related orbit

A questioning case is highlighted by some buildings also oriented to the west (circled in red Fig. 23a) but showing fewer changes with the statistical approach Orbit 21 than 116 (Fig. 23b) positioned east-side. Moreover, the signatures from two of these buildings, range from -1.8 to -9.0 z-score, and the disaster impact is striking on WV02 images (Fig. 24). Intuitively, Orbit 21 positioned west-side should be more effective, as the disaster impact is striking (Fig. 24).



(a) Smap Orbit 21: Buildings (circled in red) detect few changes - OSM ID 148707759.



(b) Smap Orbit 116: Buildings detect few more changes than orbit 21 - OSM ID 99999000064.

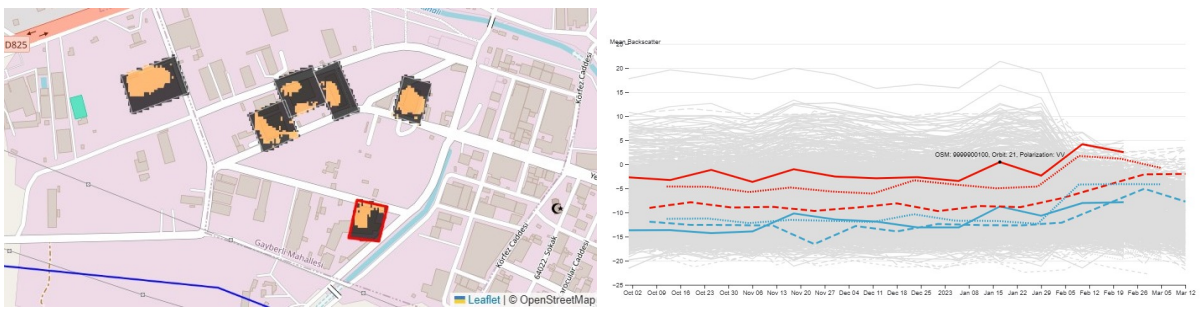
Figure 23: Start maps (`smap`) of first change for each orbit and temporal signatures of buildings with few changes, while the intensities dropped (z-scores from -1.8 to -4.0).



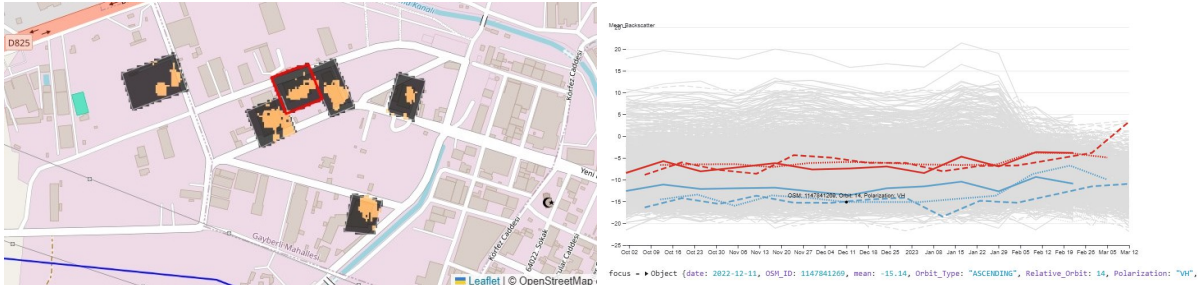
Figure 24: Disaster impact for building OSM ID 1148707759 and neighboring buildings seen with WV02 image (12/02/23). Red: CEMS 'Destroyed' graded points.

### Temporal signatures increase of trend

South of AOI04, let's examine some cases on the industrial zone - an interesting area as many changes are occurring there (Fig. 36). These examples display a consistent increase of intensity after event (Fig. 25). Other buildings signatures are shown in Fig. 40 (Appendix). The thematic maps also highlight visible changes for both orbits as the surrounding are less dense than in previous examples. Both sensors orientation are able to detect changes. Looking more closely at the buildings Fig. 26, those buildings are warehouse with large low-pitched roofs, which specular reflection deflects signal away from the sensor. When they collapse, the changes in surface angle and roughness result in increased backscattering toward the sensor. For large low-pitched roofs, the loss of specular reflection has a remarkable impact in the signature.



(a) Smap Orbit 21: Warehouse in industrial zone, with increasing intensity trend - OSM ID: 9999900100.



(b) Smap Orbit 116: Warehouse in industrial zone, with increasing intensity trend - OSM ID 1147841269).

Figure 25: Start maps (**smap**) of first change for each orbit and temporal signatures of buildings.



Figure 26: WV02 image from (12/02/23) for industrial zone and corresponding buildings. Green polygons represent OSM footprints; red and green points indicate reviewed CEMS products.

Thus, our interactive tool allows multiple possibilities according to the needs of analysis. It gives the spatial and temporal comparison of change occurrences from each approach used. Both approaches are complementary as change may be detected with one or another. Damage assessment can be conducted for each building regarding different orbit, polarization, frequency or first occurrence of change. We highlights the need to analyze the urban context regarding to sensors orientation or the shape of building roofs for example. Such interactive analysis is more suited to be used and demonstrated dynamically. Moreover, some undetected damages remains and opens the way for further research and understanding.

## 7.1. Regarding the research objective

To cover the research objective, *Assessing building damage after a seismic event using unsupervised change detection with Sentinel-1 imagery*, we investigated intensity time series across multiple acquisition dates (11 before and 2 after the event). Temporal signatures for the destroyed building footprints confirmed a change of trend in intensities before/after event, often revealing complementary signatures between polarizations and orbits: if one failed to detect a change, the other succeeded. Most destroyed buildings contain at least one signature that deviates from its trend before event. Both decreasing and increasing intensity are observed depending on the building situation.

The sequential omnibus likelihood ratio test further refined this preliminary analysis by exploiting both channels using the determinant of the dual-polarized covariance matrix to statistically detect significant shifts in the backscatter signal. This approach takes in account the statistical properties of speckled data, the multilooking process and also allows to control the false positive rate. We prove the method's efficiency to our case, detecting changes for entire sequence of images during event simultaneously over the whole destroyed buildings dataset. By sequentially evaluating changes in the covariance matrices, the method assesses the overall differences between distributions at multiple times. The sequential omnibus algorithm provides multitemporal change maps, indicating the first occurrence, most recent change, and frequency of changes, which enables to determine where and when a change has occurred in our time series. Then, we infer changes related with the disaster event using our destroyed footprints and filtering pixels where changes already occurred.

However, the change detection algorithm is purely data driven. Results vary almost complementary depending on the satellite flight direction and are reliant on the side-looking features of SAR data. This lead to a relatively high missing rate, which could also be due to filtering pixels where changes already occurred al still concerned with the disaster. One of the perspective would be to keep the accuracy from the bitemporal map and use the `fmap` of frequency of changes to characterize event-related changes.

## 7.2. About event-related works

Yu et al. (2024) multi-class damage detection model achieved a peak ROC-AUC<sup>1</sup> of 0.69 using a random forest classifier. Exploiting the joint use of optical and SAR remote sensing-derived indices significantly enhanced the accuracy of their building damage assessment. To compare, the ROC-AUC for our 2-classes Smap of first change ('Destroyed'/'Non destroyed' at event interval) is around 0.84 for each orbit. Although this is hardly comparable as in their multi-class case, lower accuracy is due to misclassification at the slight damage level.

Wang et al. (2023) additionnaly used coherence information with Sentinel-1 data, and detected around 67% of the destroyed buildings from the output of Microsoft team which leveraged artificial intelligence technology. In our case, the difficulty is to compare with the Microsoft grading which is expressed in % of damage. For doing so, a perspective could be to assess our change detection considering the surface of the footprint (surface of changed detected / total of footprint surface).

H. Liu et al. (2024) method based on a multitemporal InSAR coherence performed validation on the East Anatolia event, with a correct rate of 72.8%, 27.2% missing and 13.3% false identification, where we obtained 74.5%, 38.1% and 12.8% respectively. Our higher missing rate can be explained by the use of only one orbit, when H. Liu et al. (2024) results from the use of two. As with temporal signatures we observed a complementary response between orbits, where if one failed to detect a change, the other succeeded.

Using solely post-event SAR imagery at 0.8-m resolution also by random forest, Macchiarulo et al. (2024) achieved precision of 66% and accuracy from 73 to 83%. Comparatively, their model also suffers from recall of 72% in average, missing several instances of actual damage. Our unsupervised method performs in the same range, which is satisfying regarding the 10-m resolution. Pre-event image collection is a challenge in their case at VHR resolution, while for us it is an opportunity to assess the situation before event and filter pixels prone to change.

Overall our results are promising considering the unsupervised approach, the resolution used and the solely intensity-based approach. It is relatively straightforward, easy to implement or interpret and require no labeling data. The use of Sentinel-1 image collection at 10-m resolution is here an opportunity to exploit pre-event information.

## 7.3. Limits and perspectives

To start with, our approach stands in between the context of rapid mapping and post-event analysis because of two details: if the focus remains on post-event analysis regardless of the time

---

<sup>1</sup>The ROC-AUC is the area under the ROC (receiver operating characteristic) curve, which is computed from the True Positive Rate and False Positive Rate (see Fig. 39 in Appendix). A higher ROC-AUC value indicates better performance.

gap between acquisitions, merging results from both ascending and descending orbits could have enhanced the model's performance. On the other hand, to better align with the rapid mapping context, it would have been more appropriate to use a single post-event acquisition date for plotting temporal signatures, rather than relying on two.

The 'Spotlight mode' of Sentinel-1, tailored for specific scenarios such as disaster events, is well-suited for rapid mapping applications. Its data, provided in SLC format with both amplitude and phase, would also enhance the model's performance and accuracy. In this work, our approach was to focus on intensity-based assessment, using the diagonal-only dual polarization matrix. Incorporating phase information from SLC Sentinel-1 imagery would enhance the capability of change detection. SLC data contains both amplitude and phase information, allowing the construction of a full covariance matrix that captures phase relationships between polarizations. The GEE developers would be considering ways to ingest SLC Sentinel-1 imagery solving this problem (Canty et al., 2019). The multi-look dual polarization matrix format could then be constructed from the SLC data. Especially, the very recent activation of Sentinel-1C restores the full potential of the Sentinel-1 mission.

One of the difficulties encountered was the lack of information from the CEMS dataset products and their quality as reviewing damage assessment is time consuming. The Microsoft Team dataset is considered more reliable; however, their grading is expressed as a percentage of damage, requiring a threshold decision to determine whether a building is classified as destroyed. To compare, a perspective could be to assess our change detection regarding the surface of the footprint (surface of changed detected / total of footprint surface).

The change detection algorithm is purely data driven and unsupervised: the physical cause of detected changes must be inferred from the context. Here, we use OSM footprints to relate the presence of a building with the changes, but in conditions where data availability is lacking, there could be a need for inferring buildings position. The Loewner order could offer additional information in that regard.

The extension of the approach in Canty et al. (2020) consists of using the Loewner order to look at the direction of change. This direction is determined by the definiteness of the pairwise consecutive matrix differences: does the radar response increase, decrease, or does it change its structure/nature between the two time points. The Loewner order calculates whether the difference of the covariance matrices at the two time points is positive semidefinite, negative semidefinite, or indefinite. In that sense, we look into the "direction" of change, which can give complementary information about the type of change, maybe filter the changes not related to event (like roads or parking) or infer the building position. Here, we chose to limit our work as both increase and decrease of intensity can occur with building damage.

Moreover, I believe the pre-event information could be used more effectively in regards to the model's performance. With the `smap` of first changes, we filtered pixels where changes already occurred, but these pixels could still be concerned by the disaster. A prior change does not

necessarily exclude them from being related to the event. The challenge is to effectively characterize changes that are specifically event-related. Rather than `smap`, the frequency map `fmap` could be leveraged in concordance with the bitemporal map to build an indice of 'probability of event-related change': bitemporal changes during event w.r.t. frequency of changes.

Most of all, the performance evaluation of our model is very relying on the way of counting buildings classified as 'Destroyed'. Either the scale parameter which determines the amount of pixels to take in account, either our dataset digitalization that overestimates the number of buildings with changes unrelated to the event. The use of buffer may lead to take in account changes not related to buildings.

Finally, our metrics suggest that accuracy and the detection of true positives (TP) could still be significantly improved. In disaster response scenarios, balancing precision and recall is crucial. Precision reduces false positives, ensuring identified collapsed buildings are actually damaged. On the other hand, recall prioritizes identifying as many collapsed buildings as possible, at the cost of potential false positives. The relative importance on either metric depends on response objectives and emergency resource availability (Macchiarulo et al., 2023).

---

## 8. Conclusion

This master thesis explored an unsupervised multitemporal change detection method using Sentinel-1 imagery to assess building damages following the 2023 seismic event in East Anatolia, Turkey.

The first part of this work focused on constructing a reliable dataset of Destroyed and Non-destroyed building footprints by reviewing CEMS rapid mapping products through visual analysis of VHR optical imagery, and ancillary data such as OSM footprints.

We analyzed time series of the mean backscatter intensity for each building footprint to identify changes in trends before and after the seismic event. Significant deviations exceeding  $1\sigma$  in intensity were observed post-destruction compared to pre-destruction. Using a buffer around the footprint proved effective in detecting trend changes, particularly by accounting for the lay-over and double-bounce effects inherent in SAR data. These effects, often observed in urban environments, can cause signal distortions or enhancements at building edges and surrounding areas, which the buffer effectively captures.

Notably, when one polarization failed to detect changes, the other often succeeded. This complementarity between polarizations underscores the importance of combining information from both VV and VH channels using the covariance matrix. The sequential omnibus test leverages the determinant of the covariance matrix to compute the likelihood ratio test statistic, assessing overall differences between distributions across multiple time points. This method offers several advantages: it is unsupervised, accounts for the statistical properties of speckled data, incorporates the multilooking process inherent to SAR imagery and allow to control the false positive rate.

Then, we implemented the omnibus test to assess changes across the time series for the entire study area and within both Destroyed and Non-destroyed building footprints. Changes were effectively detected within the Destroyed footprints across the event sequence. Subsequently, a sequential algorithm of omnibus tests is used to determine where and when a change has occurred. This produces temporal change maps of the interval of change, the most recent, the first, and the frequency. We compare results of both the bitemporal map and a multitemporal map -of first change- during event compared to before event, at the city level. We infer the cause of the change related to the event using our building datasets to obtain metrics. Both maps show consistent performance with slight deviation across different levels of significance. Depending on the priority of risk assessment, the multitemporal map, avoiding pixels where changes occurred, is more interesting with its high specificity.

The process is *shared here*, linked with a Github repository hosting and sharing the reference data for free and open source to use. To support comprehensive analysis, we developed an interactive tool *available here* that integrates results from both temporal signature and the

sequential omnibus algorithm. This tool allows for comparison of our outputs at the building level across various parameters, offering insights into the strengths and limits of the approach. Overall, our results provide a benchmark for the unsupervised intensity-based approach. The method is relatively straightforward, easy to implement or interpret and require no labeling data. The use of Sentinel-1 image collection at 10-m resolution is here an opportunity to exploit pre-event information.

However, these results are highly data-driven and method-dependent, which frames the comparison with other studies on the East Anatolia event. Regarding the comparatively high missing rate from the map of first change, the use of frequency of changes would have been interesting to filter pixels prone to frequent changes.

In conclusion, the methods developed in this study enables the evaluation of changes in SAR time series. The integration of temporal signatures, statistical change detection, and interactive visualization provides a comprehensive approach to understanding the spatial and temporal distribution of building damage.

Future research could enhance this framework by incorporating additional polarimetric features, phase information from SLC data, and more advanced change detection techniques. These improvements could further support rapid disaster response and post-event analysis, contributing to more effective recovery strategies for seismic disasters.

---

## Bibliography

- Ainsworth, T., Schuler, D., & Lee, J.-S. (2008). Polarimetric sar characterization of man-made structures in urban areas using normalized circular-pol correlation coefficients. *Remote Sensing of Environment*, 112(6), 2876–2885. <https://doi.org/10.1016/j.rse.2008.02.005>
- Ajmar, A., Boccardo, P., Disabato, F., & Giulio Tonolo, F. (2015). Rapid mapping: Geomatics role and research opportunities. *Rendiconti Lincei*, 26, 63–73. <https://doi.org/10.1007/s12210-015-0410-9>
- Arai, K., Nakaoka, Y., & Okumura, H. (2024). Method for disaster area detection with just one sar data acquired on the day after earthquake based on yolov8. *International Journal of Advanced Computer Science & Applications*, 15(3). <https://doi.org/10.14569/IJACSA.2024.0150344>
- Arslan Kelam, A., Karimzadeh, S., Yousefibavil, K., Akgün, H., Askın, A., Erberik, M. A., Koçkar, M. K., Pekcan, O., & Ciftci, H. (2022). An evaluation of seismic hazard and potential damage in gaziantep, turkey using site specific models for sources, velocity structure and building stock. *Soil Dynamics and Earthquake Engineering*, 154, 107129. <https://doi.org/10.1016/j.soildyn.2021.107129>
- Brunner, D., Lemoine, G., & Bruzzone, L. (2010). Earthquake damage assessment of buildings using vhr optical and sar imagery. *IEEE Transactions on Geoscience and Remote Sensing*, 48(5), 2403–2420. <https://doi.org/10.1109/TGRS.2009.2038274>
- Canty, M. (2024). *Detecting changes in sentinel-1 imagery, part 3* [Accessed: 2024-08-17]. <https://developers.google.com/earth-engine/tutorials/community/detecting-changes-in-sentinel-1-imagery-pt-3>
- Canty, M., Nielsen, A. A., Conradsen, K., & Skriver, H. (2019). Statistical analysis of changes in sentinel-1 time series on the google earth engine. *Remote Sensing*, 12(1), 46. <https://doi.org/10.3390/rs12010046>
- Colin, E. (2023). Poltimesar: Why we need full polarimetry to detect changes in a sar time series. <https://hal.science/hal-04011052>
- Conradsen, K., Nielsen, A. A., & Skriver, H. (2016). Determining the points of change in time series of polarimetric sar data. *IEEE Transactions on Geoscience and Remote Sensing*, 54(5), 3007–3024. <https://doi.org/10.1109/TGRS.2015.2510160>
- Cooner, A. J., Shao, Y., & Campbell, J. B. (2016). Detection of urban damage using remote sensing and machine learning algorithms: Revisiting the 2010 haiti earthquake. *Remote Sensing*, 8(10), 868. <https://doi.org/10.3390/rs8100868>
- Cotrufo, S., Sandu, C., Giulio Tonolo, F., & Boccardo, P. (2018). Building damage assessment scale tailored to remote sensing vertical imagery. *European Journal of Remote Sensing*, 51(1), 991–1005. <https://doi.org/10.1080/22797254.2018.1527662>

- Dell'Acqua, F., & Gamba, P. (2012). Remote sensing and earthquake damage assessment: Experiences, limits, and perspectives. *Proceedings of the IEEE*. <https://doi.org/10.1109/JPROC.2012.2196404>
- Dong, L., & Shan, J. (2013). A comprehensive review of earthquake-induced building damage detection with remote sensing techniques. *ISPRS Journal of Photogrammetry and Remote Sensing*, 84, 85–99. <https://doi.org/10.1016/j.isprsjprs.2013.06.011>
- Du, Y.-N., Feng, D.-C., & Wu, G. (2024). Insar-based rapid damage assessment of urban building portfolios following the 2023 turkey earthquake. *International Journal of Disaster Risk Reduction*, 103, 104317. <https://doi.org/10.1016/j.ijdrr.2024.104317>
- ESA. (2024). *Sentinel toolbox and documentation* [Accessed: 2024-08-17]. <https://sentiwiki.copernicus.eu/web/>
- Flores-Anderson, A. I., Herndon, K. E., Thapa, R. B., & Cherrington, E. (2019). The synthetic aperture radar (sar) handbook: Comprehensive methodologies for forest monitoring and biomass estimation. <https://doi.org/10.25966/NR2C-S697>
- Ge, P., Gokon, H., & Meguro, K. (2020). A review on synthetic aperture radar-based building damage assessment in disasters. *Remote Sensing of Environment*, 240, 111693. <https://doi.org/10.1016/j.rse.2020.111693>
- Ghaffarian, S., Rezaie Farhadabad, A., & Kerle, N. (2020). Post-disaster recovery monitoring with google earth engine. *Applied Sciences*, 10(13), 4574. <https://doi.org/10.3390/app10134574>
- Gong, L., Wang, C., Wu, F., Zhang, J., Zhang, H., & Li, Q. (2016). Earthquake-induced building damage detection with post-event sub-meter vhr terrasar-x staring spotlight imagery. *Remote Sensing*, 8(11), 887. <https://doi.org/10.3390/rs8110887>
- Guida, R., & Brett, P. T. (2011). A sar image-based tool for prompt and effective earthquake response. *2011 Joint Urban Remote Sensing Event*, 213–216. <https://doi.org/10.1109/JURSE.2011.5764758>
- Joyce, K. E., Belliss, S. E., Samsonov, S. V., McNeill, S. J., & Glassey, P. J. (2009). A review of the status of satellite remote sensing and image processing techniques for mapping natural hazards and disasters. *Progress in physical geography*, 33(2), 183–207. <https://doi.org/10.1177/0309133309339563>
- Kaku, K. (2019). Satellite remote sensing for disaster management support: A holistic and staged approach based on case studies in sentinel asia. *International Journal of Disaster Risk Reduction*, 33, 417–432. <https://doi.org/10.1016/j.ijdrr.2018.09.015>
- Liu, H., Song, C., Li, Z., Liu, Z., Ta, L., Zhang, X., Chen, B., Han, B., & Peng, J. (2024). A new method for the identification of earthquake-damaged buildings using sentinel-1 multi-temporal coherence optimized by homogeneous sar pixels and histogram matching. *IEEE Journal of Selected Topics in Applied Earth Observations and Remote Sensing*. <https://doi.org/10.1109/JSTARS.2024.3377218>

- Liu, J., Huang, C., Zhang, G., Shan, X., Korzhenkov, A., & Taymaz, T. (2024). Immature characteristics of the east anatolian fault zone from sar, gnss and strong motion data of the 2023 türkiye–syria earthquake doublet. *Scientific Reports*, 14(1), 10625. <https://doi.org/10.1038/s41598-024-61326-6>
- Liu, W., Yang, J., Zhao, J., Shi, H., & Yang, L. (2018). An unsupervised change detection method using time-series of polsar images from radarsat-2 and gaofen-3. *Sensors*, 18(2), 559. <https://doi.org/10.3390/s18020559>
- Macchiarulo, V., Foroughnia, F., Milillo, P., Whitworth, M. R., Penney, C., Adams, K., Kijewski-Correa, T., & Giardina, G. (2023). City-scale damage assessment using very-high-resolution sar satellite imagery and building survey data for the 2021 haiti earthquake.
- Macchiarulo, V., Giardina, G., Milillo, P., Aktas, Y. D., & Whitworth, M. R. (2024). Integrating post-event very high resolution sar imagery and machine learning for building-level earthquake damage assessment. *Bulletin of Earthquake Engineering*, 1–27. <https://doi.org/10.1007/s10518-024-01877-1>
- Malmgren-Hansen, D., Sohneseen, T., Fisker, P., & Baez, J. (2020). Sentinel-1 change detection analysis for cyclone damage assessment in urban environments. *Remote Sensing*, 12(15), 2409. <https://doi.org/10.3390/rs12152409>
- Matin, S. S., & Pradhan, B. (2022). Challenges and limitations of earthquake-induced building damage mapping techniques using remote sensing images-a systematic review. *Geocarto International*, 37(21), 6186–6212. <https://doi.org/10.1080/10106049.2021.1933213>
- Matsuoka, M., & Yamazaki, F. (2004). Use of satellite sar intensity imagery for detecting building areas damaged due to earthquakes. *Earthquake Spectra*, 20(3), 975–994. <https://doi.org/10.1193/1.1774182>
- Mazzanti, P., Scancella, S., Virelli, M., Frittelli, S., Nocente, V., & Lombardo, F. (2022). Assessing the performance of multi-resolution satellite sar images for post-earthquake damage detection and mapping aimed at emergency response management. *Remote Sensing*, 14(9), 2210. <https://doi.org/10.3390/rs14092210>
- Moreira, A., Prats-Iraola, P., Younis, M., Krieger, G., Hajnsek, I., & Papathanassiou, K. P. (2013). A tutorial on synthetic aperture radar. *IEEE Geoscience and remote sensing magazine*, 1(1), 6–43. <https://doi.org/10.1109/MGRS.2013.2248301>
- Nascimento, A. D., Frery, A. C., & Cintra, R. J. (2018). Detecting changes in fully polarimetric sar imagery with statistical information theory. *IEEE Transactions on Geoscience and Remote Sensing*, 57(3), 1380–1392. <https://doi.org/10.1109/TGRS.2018.2866367>
- Plank, S. (2014). Rapid damage assessment by means of multi-temporal sar—a comprehensive review and outlook to sentinel-1. *Remote Sensing*, 6(6), 4870–4906. <https://doi.org/10.3390/rs6064870>
- Rao, A., Jung, J., Silva, V., Molinario, G., & Yun, S.-H. (2023). Earthquake building damage detection based on synthetic-aperture-radar imagery and machine learning. *Natural Haz-*

- ards and Earth System Sciences*, 23(2), 789–807. <https://doi.org/10.5194/nhess-23-789-2023>
- Salepci, N., Eckardt, R., & Richter, N. (2017). Speckle filtering—basics, concepts & techniques. *Germany: Friedrich-Schiller-Universität Jena.*
- Voigt, S., Kemper, T., Riedlinger, T., Kiefl, R., Scholte, K., & Mehl, H. (2007). Satellite image analysis for disaster and crisis-management support. *IEEE transactions on geoscience and remote sensing*, 45(6), 1520–1528. <https://doi.org/10.1109/TGRS.2007.895830>
- Wang, Feng, G., He, L., An, Q., Xiong, Z., Lu, H., Wang, W., Li, N., Zhao, Y., Wang, Y., et al., (2023). Evaluating urban building damage of 2023 kahramanmaraş, turkey earthquake sequence using sar change detection. *Sensors*, 23(14), 6342. <https://doi.org/10.3390/s23146342>
- Yang, Xie, C., Tian, B., Guo, Y., Zhu, Y., Yang, Y., Fang, H., Bian, S., & Zhang, M. (2024). Large-scale building damage assessment based on recurrent neural networks using sar coherence time series: A case study of 2023 turkey–syria earthquake. *Earthquake Spectra*, 40(4), 2285–2305. <https://doi.org/10.1177/87552930241262761>
- Yousif, O., & Ban, Y. (2016). Object-based change detection in urban areas using multitemporal high resolution sar images with unsupervised thresholding algorithms. In *Multitemporal remote sensing: Methods and applications* (pp. 89–105). Springer. [https://doi.org/10.1007/978-3-319-47037-5\\_5](https://doi.org/10.1007/978-3-319-47037-5_5)

---

# Appendix

---

## Appendix A:

### Implementation

**Google Earth Engine** The process was developed on Google Earth Engine (GEE) via a Colaboratory Notebook. GEE is widely used as cloud computing platform for Remote Sensing (RS) Big Data applications, as described in Amani's (2020) comprehensive review. Most of the developed RS-based approaches in post-disaster damage and recovery assessments use high-resolution data that require extensive digital storage and computing capacity (Ghaffarian et al., 2020). GEE platform provides appropriate solution for these needs and the Python API's can be programmed to analyze time series of Sentinel-1 acquisitions.

b The complete Colaboratory Notebook developed is available here.

It takes for inputs the AOIs and the dataset of 375 'Destroyed' (OSM\_batch1) and Non-Destroyed (OSM\_batch2) buildings footprints with 20m buffers (respectively OSM\_buffer20 and OSM\_2 buffer20) as GeoJSON. After processing, the outputs are extracted and uploaded to the ObservableHQ notebook.

**ObservableHQ Notebook** To present these outputs and enable interactive analysis, a Notebook on ObservableHQ was created. This tool was developed using D3.js, a javascript library for data visualization. It allows the dynamic analysis between the temporal signatures from destroyed buildings and the change maps output, across various parameters (polarization, orbit, z-scores and significance level).

The complete ObservableHQ Notebook developed is available here:

<https://observablehq.com/@ulgeovisualization/damage-assessment-using-sar>

The map displays different layers of change maps to select. They are clipped to the buildings footprints to enable contextual analysis with OSM background map. A click on a footprint highlights its temporal signature, and vice-versa, a click on a temporal signature zooms on the related footprint. This tool aids in a comprehensive understanding of the spatial and temporal distribution of changes, in relation to disaster damage, according to these parameters.

## A.1.1: Intensity temporal signatures of Destroyed building

**Dataset & parameters definition** defines the AOIs, the dataset of buildings footprint and the parameters such as 'Polarization' and disaster event date.

**Sentinel-1 Image collection** builds the Sentinel-1 ground range detected images collection and display their imprint (Figure 17) along with the AOIs and buildings dataset.

**Buildings Signatures dataframe** creates a dataframe of the temporal signatures for each 'Destroyed' building footprint, for each relative orbit and polarization.

The function `get_time_series` extracts the time series of mean values intensity for a given geometry from a collection of images. With 10x10 m<sup>2</sup> pixels of Sentinel-1, the building footprints may overlap several pixels. When so, `reduceRegion()` will weight the contribution of each pixel by the fraction of the pixel area covered by the geometry.

The function `to_db` converts the radar backscatter values from linear scale to decibel (dB) scale, enhancing the interpretability of the data. The dB scale is logarithmic, meaning it can better represent the wide range of radar backscatter intensities, as seen in Chapter II.

The remaining script organizes the data. The function `fc_to_df` converts a collection of features (geometries) and their respective time series into a Pandas dataframe to comply with Altair, a visualization library for Python. The function `df_by_orbit` organizes the time series by relative orbit number. The commands process those functions for our image collections on both VV and VH polarizations and combines the results in a final dataframe

For each of the 375 Destroyed building, there are two polarizations with three relative orbits, for a total of 2250 signatures. Over our timeframe of 13 dates, it will give a total of 29 250 values: the mean intensity over the footprint geometry at instant t. This dataframe will be the input for the interactive charts described below.

The next sub-section presents the final tool of Section I, an **interactive chart** displaying our final dataframe, the mean intensity for each building footprint over time, with distinct polarization types, relative orbits. The `create_combined_chart` function uses Altair library for interactive visualization tools. We programmed a different option for example to observe only one relative orbit. The **Observable HQ Notebook** will be more suitable for data visualization and such options filtering.

The **z-score** sub-section measures deviations from temporal signatures obtained. We perform a z-score standardization to identify and observe deviations ( $\sigma$ ) in building signatures after the event compared to the mean of values before : `calculate_means` splits the dataframe in before and after event date, to measure the mean of each part. `calculate_stats` measures the standard deviation for the before event part. `calculate_z_scores` measures the Z-score, as the difference in means after the event compared to before, relatively to the variability (+/- 1, 2 or  $\sigma$ ) before the event. We chose to observe the signature immediately after the event (three weeks up to one month) to catch the rubles as they appear on rapid mapping imagery.

We obtained the percentage of signatures inside a range of z-scores in Table 4 to ??, decomposed by polarizations and relative orbit. We ran the model on both 20m buffer and no-buffer footprints datasets, all along the analysis including Section II. The Observable HQ Notebook also offers filtering by range of z-scores, allowing complementary analysis with the Change Detection output from Section II.

## A.2: Multitemporal unsupervised change detection

Sub-section **Merged image lists** merges the images from a same collection that cover two different imprints at the same date, and convert them to lists for a convenient use further. Here, we select the `im_list` from the orbit we want to work on. Let's start with orbit 116 ASC, as results of z-scores Table ?? seem outstanding.

Sub-section **An omnibus test**) introduces the omnibus test for change, starting with the easier single polarization case  $S_{vv}$  (cf. Chapter 3.5). The goal here is to calculate the omnibus test statistic for each pixel's intensity up to a given time (when a change is detected) and compare the frequency of the values obtained to a theoretical chi-square distribution.

The `omnibus` function calculates the test statistic Eq. 5.8 for a list of single polarization images. The next part compare the results of the tests with the theoretical distribution, for both our buildings footprint lists, Destroyed and Non-Destroyed, as well as the whole AOIs for reference as urban area. We do so for both the 10 first images which are all before the event, and for the 3 last, which are one before and two after the event.

The function `get_histogram` computes a histogram of the omnibus test statistic values while the `norm_histogram` normalizes the frequencies. `Create_histogram` allows an interactive visualization to display all distributions datasets separately.

Next subsection builds **the sequential omnibus algorithm** using the dual polarization case. We will now use Eq. 5.12 and 5.13 to determine when changes occurred at each pixel location.

The approach taken in the coding of this algorithm is to pre-calculate P values for all of the  $Q^\ell/R_j$  tests and then, in a second pass, to filter them to determine the points of change.

The following code cell performs map operations on the indices  $\ell$  and  $j$ , returning an array of P values for all possible LRT statistics.

The program actually operates on the logarithms of the test statistics, Equation 5.8.

The function `det` calculates determinant of 2x2 diagonal covariance matrix, combining both polarizations values.

The function `log_det_sum` returns  $\log$  of determinant of the sum of the first  $j$  images  $\log \left| \sum_{i=1}^j c_i \right|$  in `im_list`, while `log_det`, returns it for the  $j^{\text{th}}$  image  $\log |c_j|$

The function `pval` calculates test statistic  $-2 \log R_j$  (from Eq. 5.8) and its corresponding p-value for the first ' $j$ ' images in `im_list` using the CDF of the chi-squared distribution

The function `p_values` pre-calculates an array of p-values for  $k - 1 + 1$  to  $k$  sequences. For each sub-series:

- iterating over different values of  $j$ , calculating the p-value and  $-2 \log R_j$  using the `pval` function,
- summing the  $-2 \log R_j$  values to calculate  $-2 \log Q_\ell$ ,
- calculate the overall p-value  $pvQ1$  from  $-2 \log Q1$  and aggregate them for all combinations of  $\ell$  and  $j$  into an array and returning this array.

The pre-calculated P values in `pv_arr` are then scanned in nested iterations over indices  $i$  and  $j$  to determine the following thematic change maps:

Therefore, `filter_j` and `filter_i` functions calculate change maps by iterating over the  $j$  indices and over row-indices of `pv_arr`, respectively. They are part of the nested iteration process to compute change maps from a pre-calculated array of P values (`pv_arr`).

To sum up, the `change_maps` function ties the overall structure. After initialization of all pixels at 0, it iterates over each row of the P values array, calling `filter_i` for each row. Within each row, `filter_i` iterates over each column, calling `filter_j` for each column. `filter_j` processes each P value, evaluates the test condition, and updates the change maps accordingly. The updated state is propagated back up through the nested iterations, ensuring that the final maps reflect all detected changes.

---

## Appendix B:

### Figures

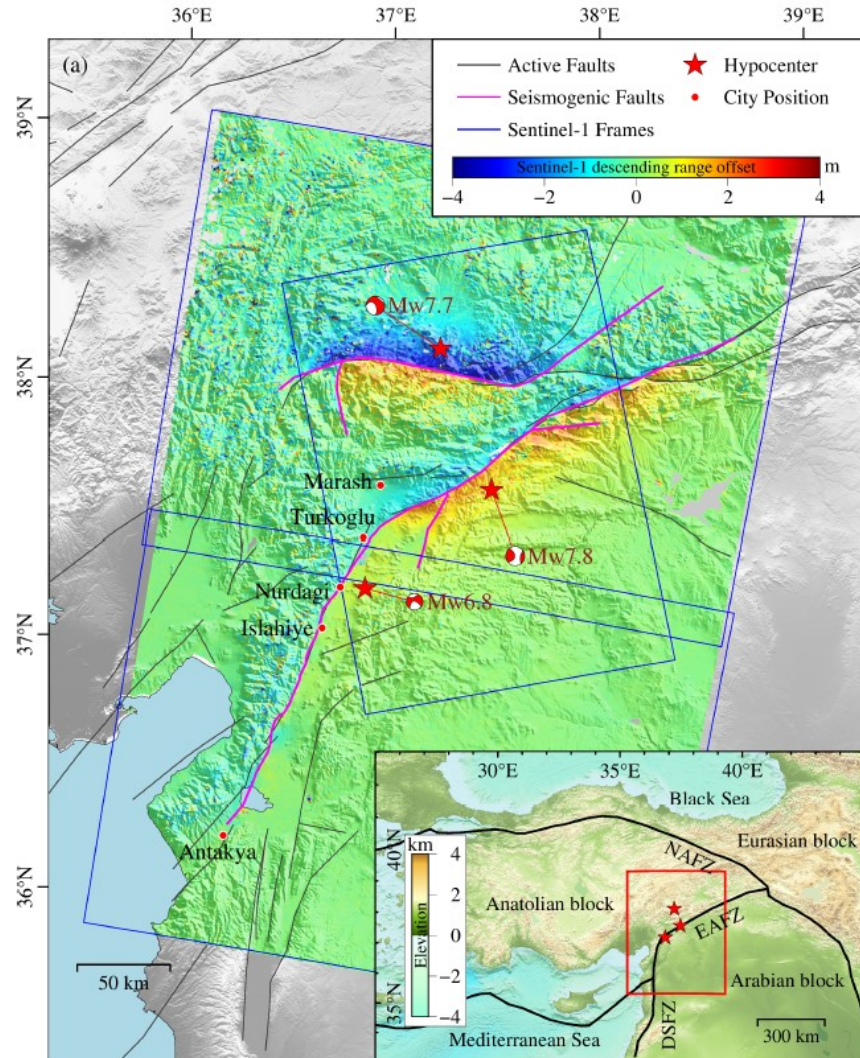


Figure 27: Surface deformation of the EAFZ seismogenic faults; the red pentagrams indicate the epicenter of the two main earthquakes and the Mw6.8 aftershock. The inset shows the regional tectonic setting: the black line is the fault zone; the north one is North Anatolian fault zone (NAFZ); the south are East Anatolian fault zone (EAFZ) and the Death Sea fault zone(DSFZ). The red stars are the epicenters (J. Liu et al., 2024).

## Appendix B. Figures

---

Frequency Band	Ka	Ku	X	C	S	L	P
Frequency [GHz]	40–25	17.6–12	12–7.5	7.5–3.75	3.75–2	2–1	0.5–0.25
Wavelength [cm]	0.75–1.2	1.7–2.5	2.5–4	4–8	8–15	15–30	60–120

Figure 28: Commonly used radar wavebands and frequency associated. Sentinel-1 uses the C-band (5.405 GHz) (Moreira et al., 2013).

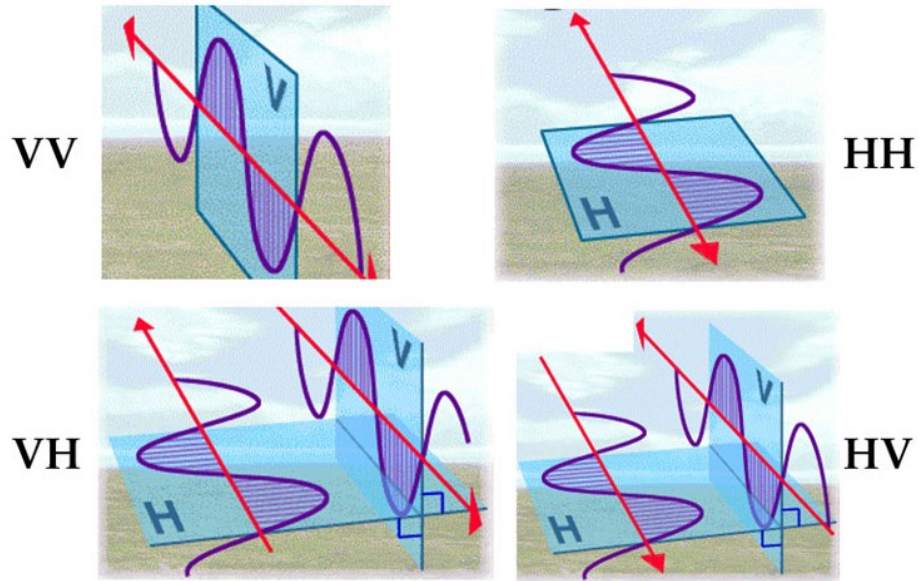
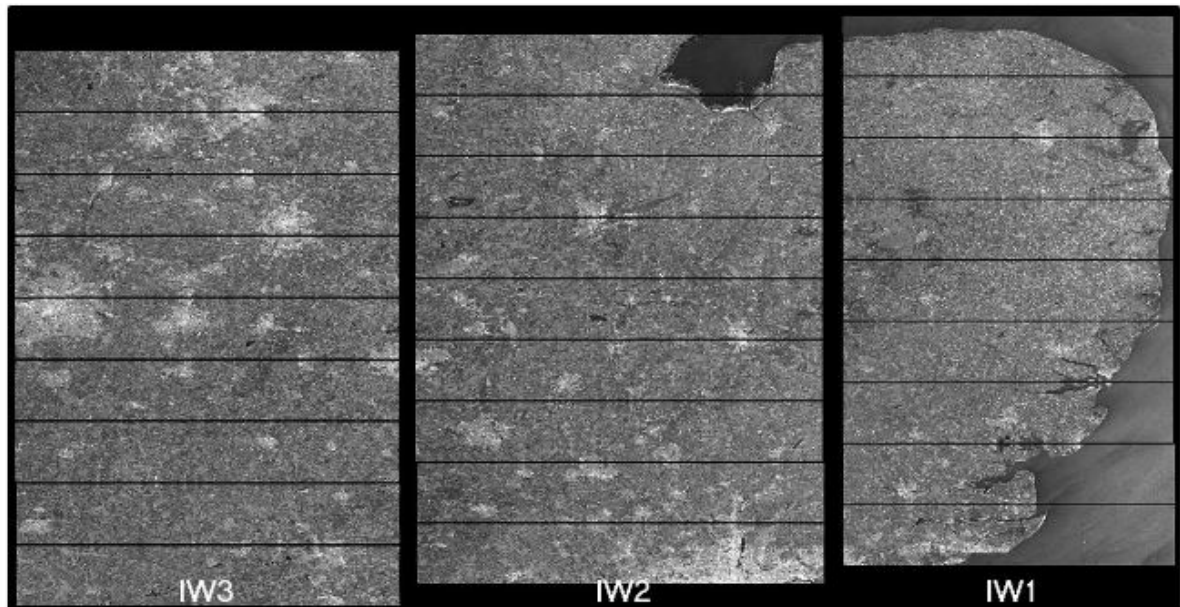


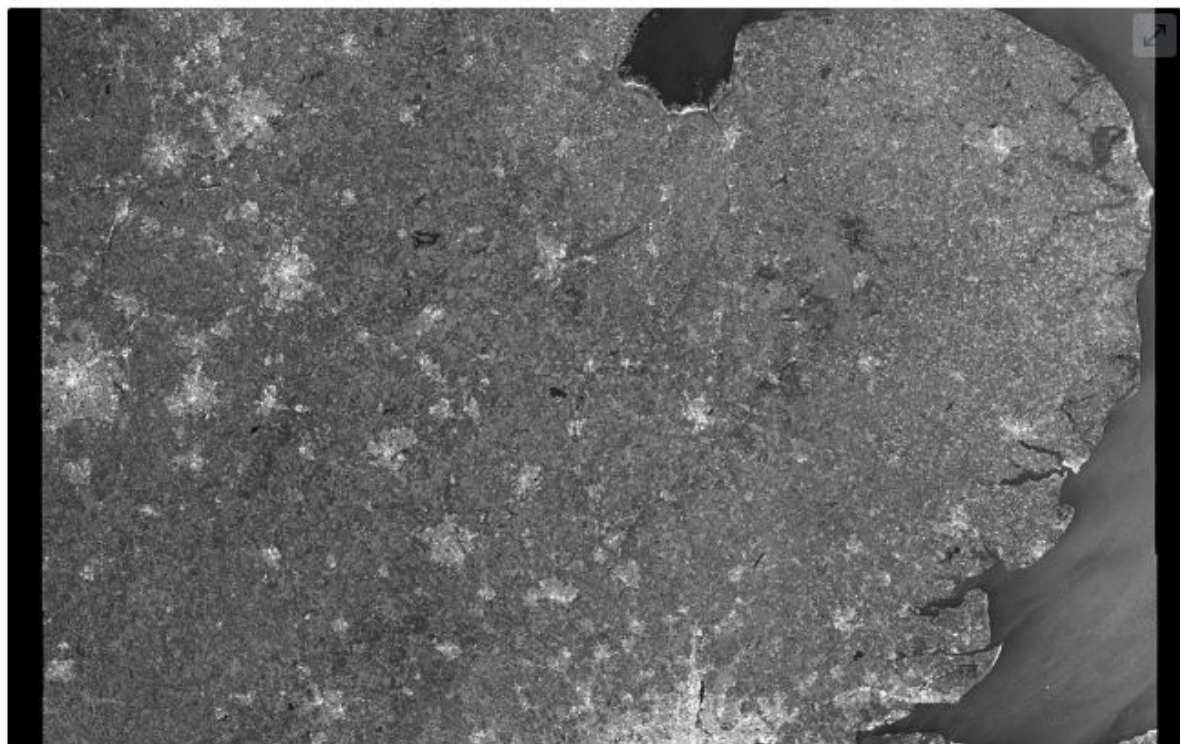
Figure 29: Polarization settings define how waves are transmitted and received (ESA, 2024).

Appendix B. Figures

---



a) IW SLC Bursts and Sub-Swaths



b) IW GRD High Resolution product

Figure 30: From SLC to GRD product (ESA, 2024).

## *Map Information*

---

A 7.8-magnitude quake struck just after 4 a.m. Monday morning local time, 23 kilometers (14.2 miles) east of Nurdagi, Gaziantep province. It is one of the strongest earthquakes to hit Republic of Türkiye in more than 100 years. The event caused dozens of collapsed buildings and fatalities. GDACS ID: EQ1357591

The present map shows the earthquake damage grade assessment in the area of Gaziantep (Türkiye). The thematic layer has been derived from post-event satellite image using a semi-automatic approach OR by means of visual interpretation. Please be aware that the thematic accuracy might be affected by the suboptimal off-nadir angle. The scale of analysis is 1:10000. The estimated geometric accuracy (RMSE) is 2.5 m or better, from native positional accuracy of the background satellite image. The minimum mapping unit (MMU) is 100 m.

## *Relevant date records (UTC)*

---

Event	06/02/2023 01:17	Situation as of	11/02/2023 08:18
Activation	06/02/2023 04:43	Map production	12/02/2023

## *Data sources*

---

Pre-event image: ESRI World Imagery © DigitalGlobe (acquired on 27/09/2021, GSD 0.6 m, approx. 0% cloud coverage in AOL).

Post-event image: WorldView-2 © Maxar Technologies, Inc. (2023), (acquired on 08/02/2023 at 09:01 UTC, GSD 0.5 m, approx. 0.0% cloud coverage in AOL, 41.6° off-nadir angle), provided under COPERNICUS by the European Union, ESA and European Space Imaging, all rights reserved.

Pléiades-1A/B © CNES (2023), distributed by Airbus DS (acquired on 11/02/2023 08:18 UTC, GSD 0.5 m, approx. 0% cloud coverage in AOL, 42.3° off-nadir angle), provided under COPERNICUS by the European Union and ESA, all rights reserved.

Base vector layers: OpenStreetMap © OpenStreetMap contributors (2022), Wikimapia.org,

Figure 31: Informations from CEMS ready-to-use map for AOI01

## Detection methods

### Detection Methods

#### *Photo-interpretation*

The analysis of the satellite imagery is manually conducted without the support of automatic processes. This method is usually applied when a more complex analytical approach is required (change detection starting from different sensor data, interpretation through interpolation by looking at neighbouring elements, identification of elements with non-homogeneous radiometric responses). A representative analysis based on the photo-interpretation method is the building damage assessment based on Very High Resolution images.

#### *Semi-automatic extraction*

The analysis of satellite imagery is conducted using supervised automatic classification. This approach is usually applied where the event generate a quite standard results in terms of radiometric response.

This methodology works well when there are available multi-temporal images with the same sensor or resolution. This approach is common for the analysis of Forest Fires based on optical satellite data to identify and to classify the burnt areas. This approach is usually used also in the identification of the flooded areas based on SAR High Resolution image.

#### *Automatic extraction*

The analysis of satellite imagery is conducted using automatic methods. This approach is usually applied where the event generate a high standard results in terms of radiometric response.

This methodology allows to reach high accuracy when the multi-temporal images with the same sensor and resolution are available.

This method is rarely used in the rapid mapping context because it is not common to guarantee homogeneity between pre and post-event data.

#### *Modelling*

The analysis of satellite imagery is conducted by Semi-automatic/Automatic methods using decision algorithm based on initial rules recalibrated by means of truth comparison.

Figure 32: CEMS methods description

EMSR648\_AOIxx\_GRA\_MONITxx\_builtUp\_r1\_v1, that corresponds to:

- The activation number [EMSR] denoting the sequential Rapid Mapping activation.
- The map-set extent defined by the area of interest identifier [AOI NUMBER].
- The product type [GRA] for grading.
- Whether it is [PRODUCT], or [MONIT], in which case updated maps are supplied at given periodic intervals. The two-digit sequential code denotes the number of the monitoring in chronological order.
- The [builtUp] specifies the assets for building footprints or point location.
- The product release [R] corresponds to 1 for the first release, and [V] for the product version. For each vector package, we chose the latest version possible amongst all.

Figure 33: Explanation of CEMS naming convention from  
<https://emergency.copernicus.eu/mapping/ems/file-naming>

## Appendix B. Figures

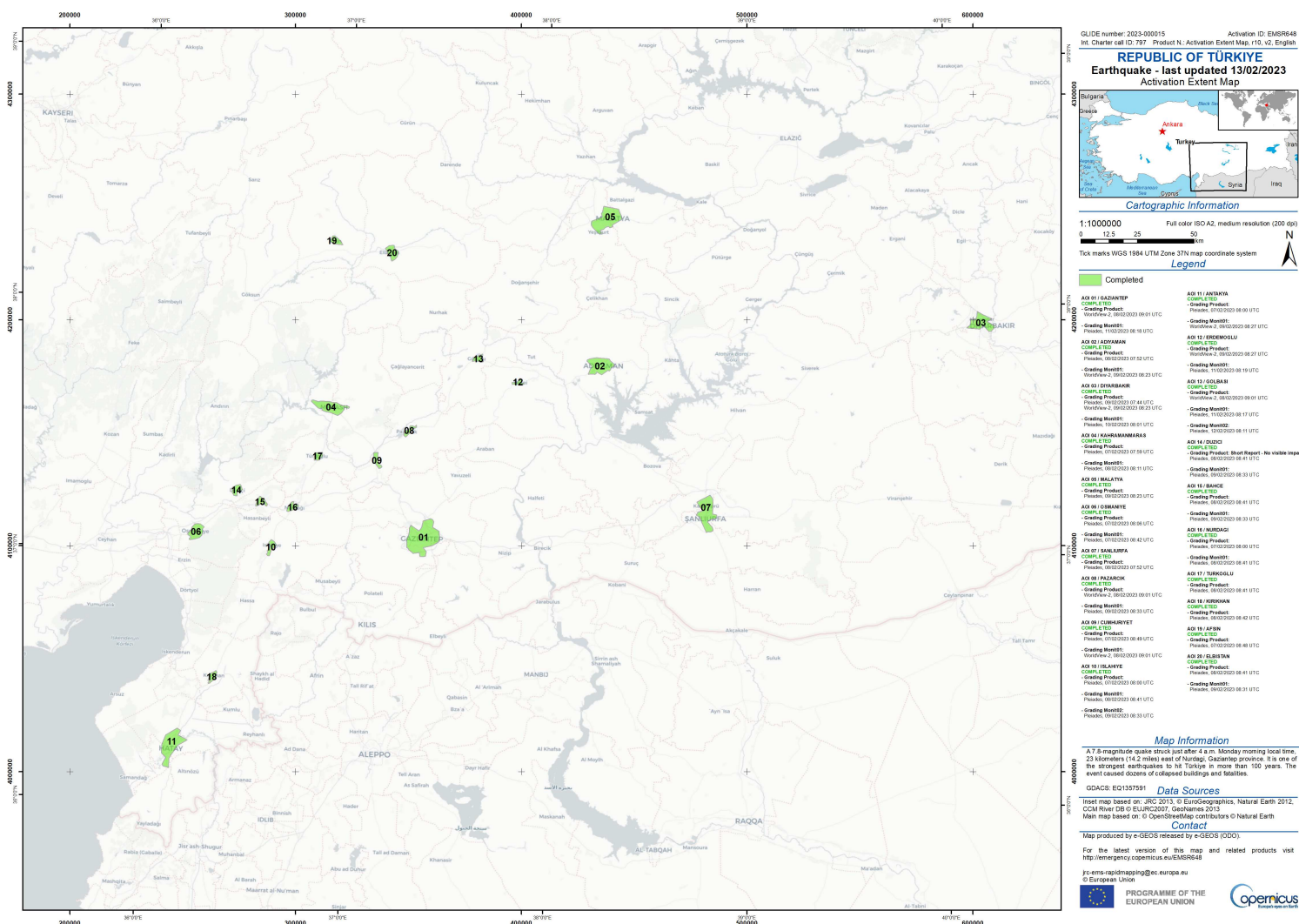


Figure 34: EMSR648 Activation Extent Map from CEMS.

Appendix B. Figures

## Appendix B. Figures

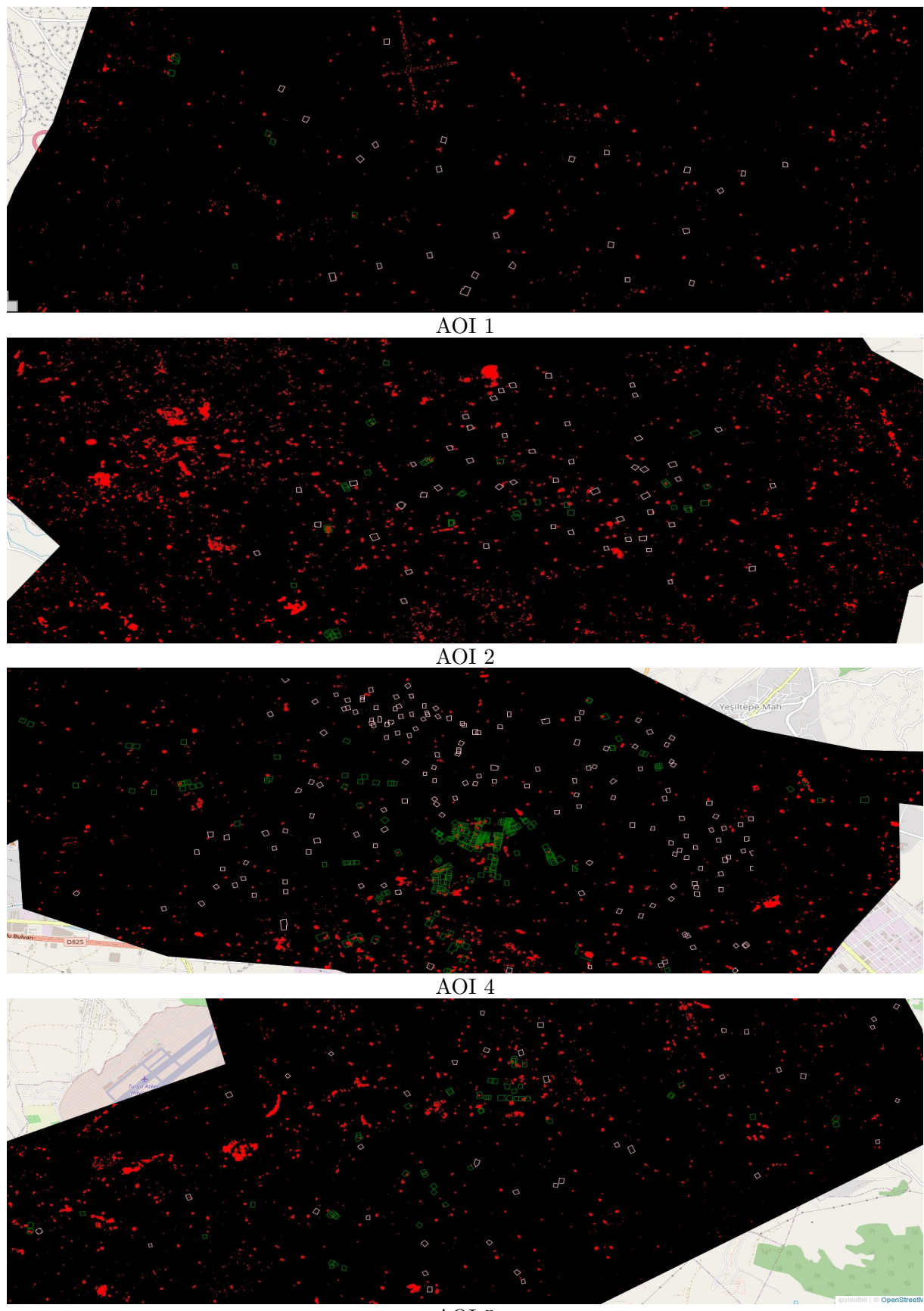


Figure 35: Bitemporal map bmap of changes detected at the interval During event for each AOI.  
Red: changes; green: 'Destroyed' footprints; white : 'Non-Destroyed' footprints.

## Appendix B. Figures

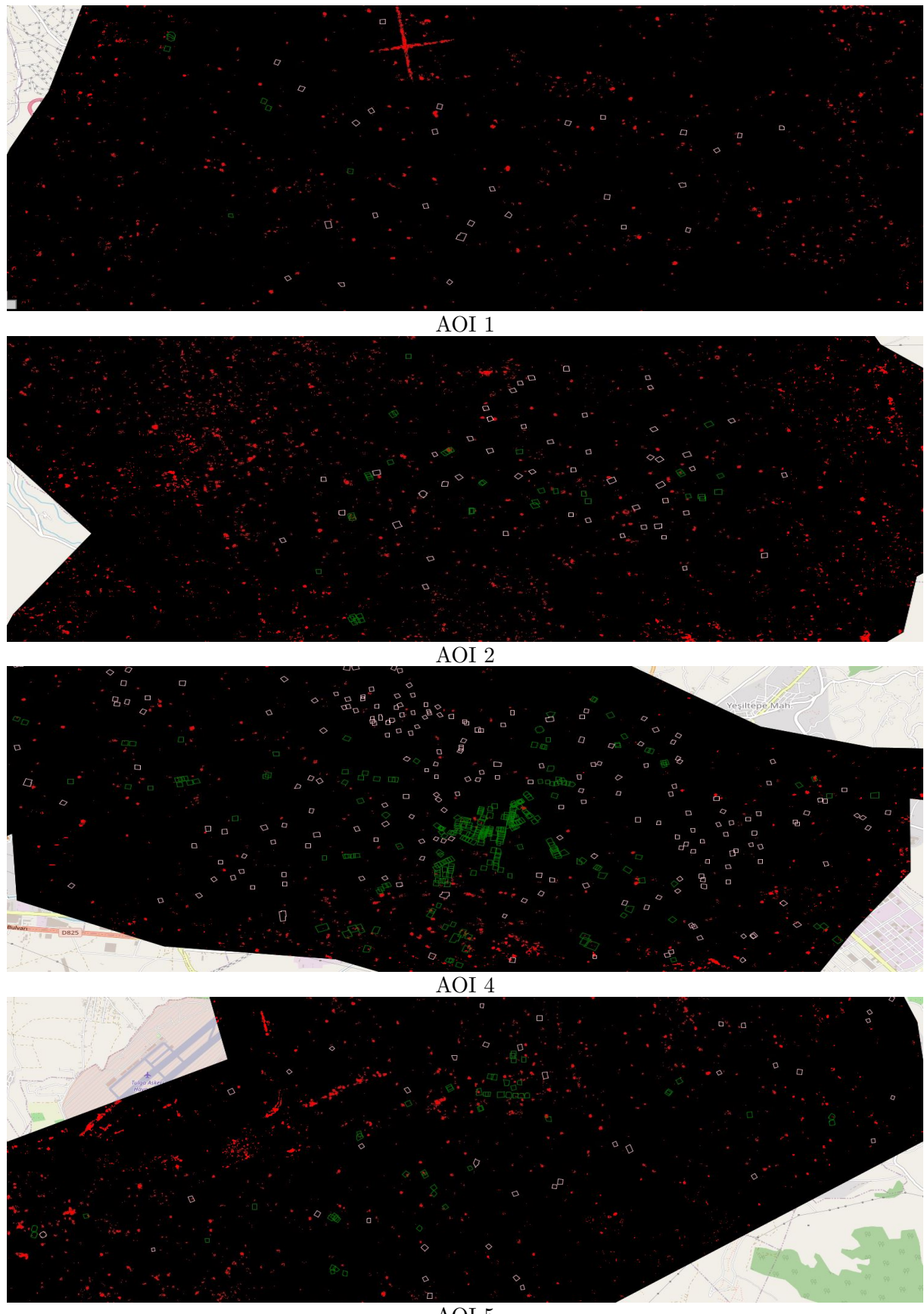


Figure 36: Bitemporal map bmap of changes detected at the interval Before event for each AOI.  
Red: changes; green: 'Destroyed' footprints; white : 'Non-Destroyed' footprints.

## Appendix B. Figures

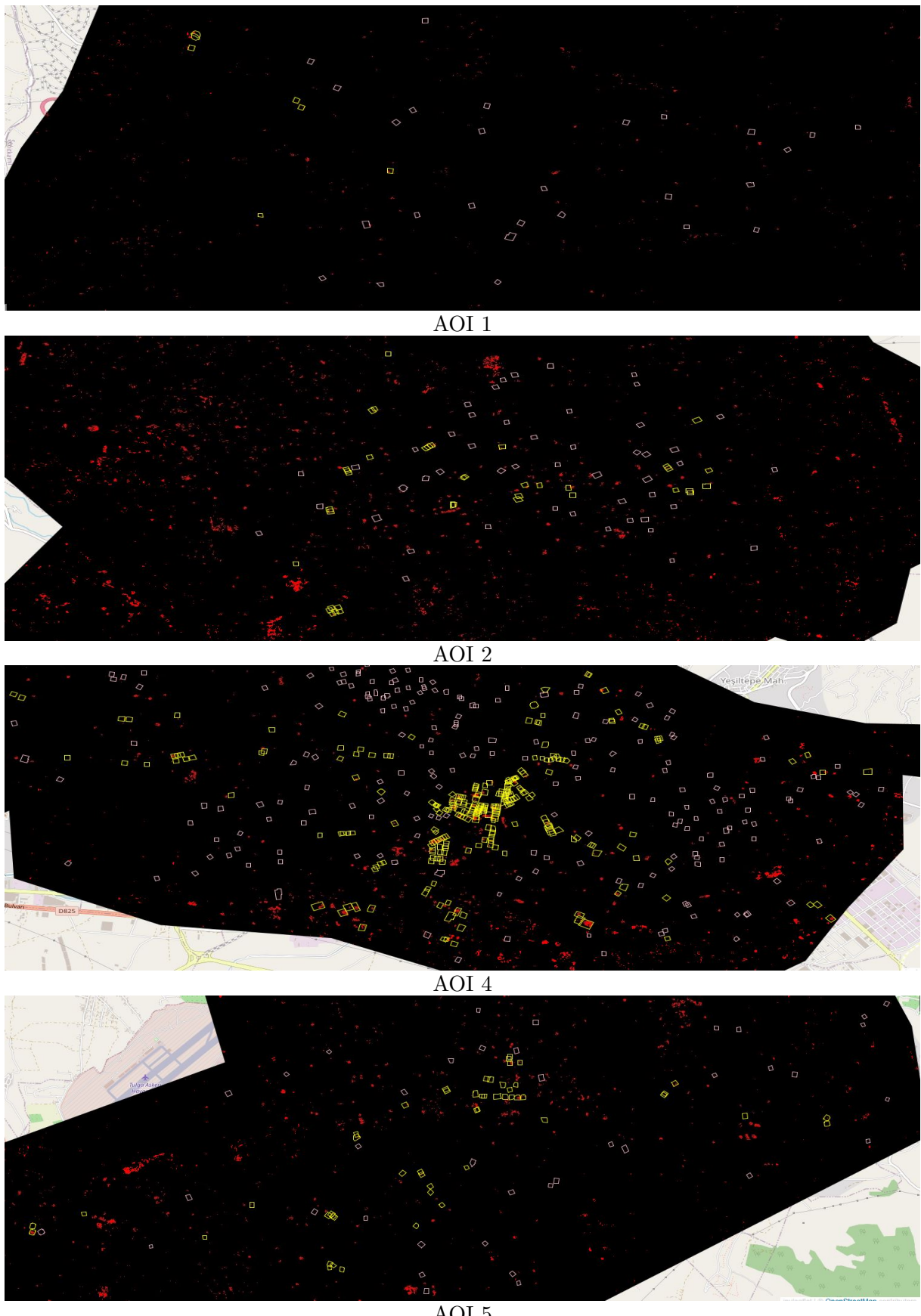


Figure 37: Map of first occurrence of change (`smap`) at the interval During event for each AOI.

Red: changes; yellow: 'Destroyed' footprints; white : 'Non-Destroyed' footprints.

## Appendix B. Figures

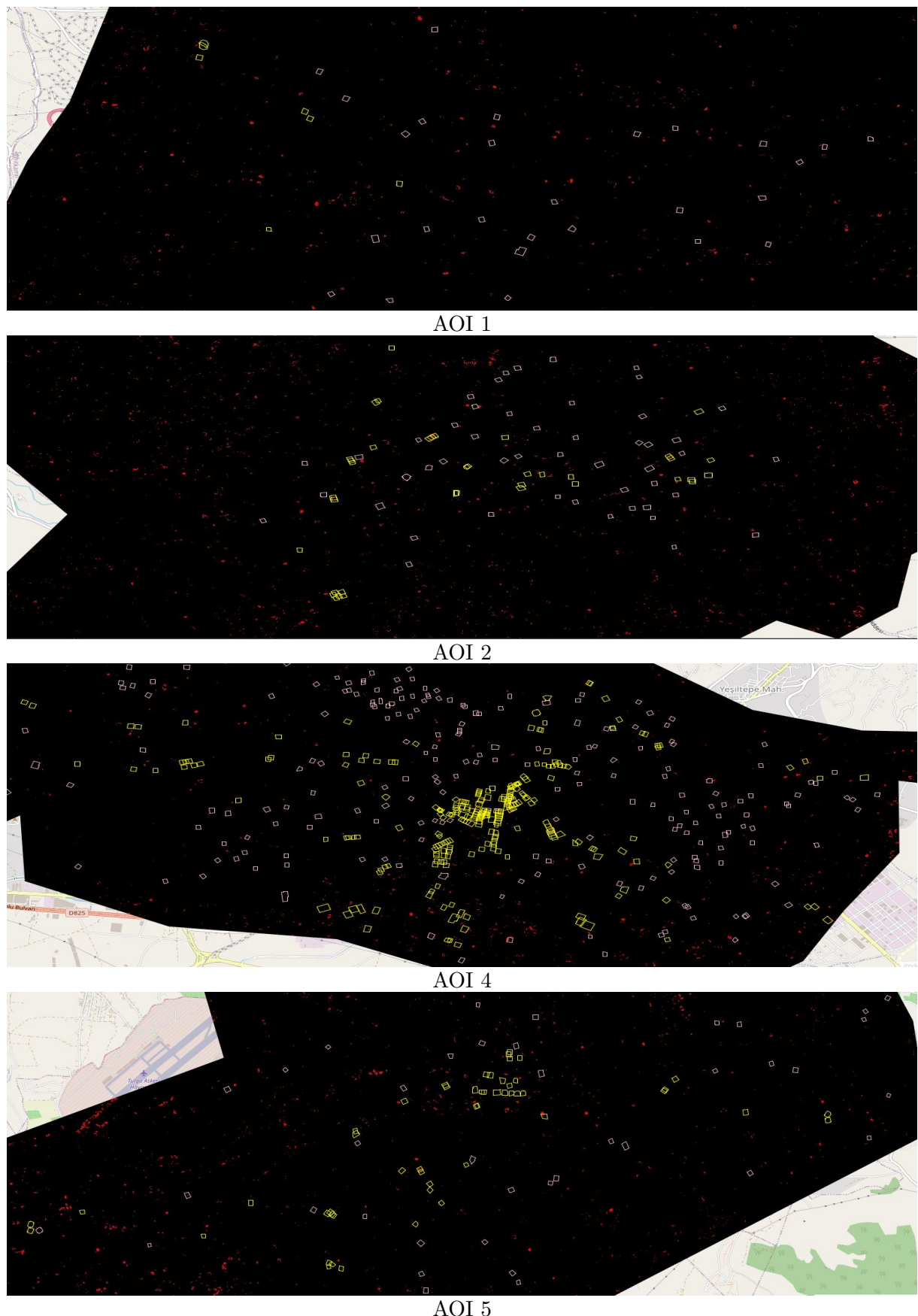


Figure 38: Map of first occurrence of change (`smap`) at the interval Before event for each AOI.

Red: changes; yellow: 'Destroyed' footprints; white : 'Non-Destroyed' footprints.

## Appendix B. Figures

---

### Metrics

$$\text{Precision} = \frac{TP}{TP + FP}$$

$$\text{Recall} = \frac{TP}{TP + FN}$$

$$\text{F1 Score} = 2 \times \frac{\text{Precision} \times \text{Recall}}{\text{Precision} + \text{Recall}}$$

$$\text{Accuracy} = \frac{TP + TN}{TP + TN + FP + FN}$$

$$\text{Specificity} = \frac{TN}{TN + FP}$$

$$\text{True Positive Rate} = \frac{TP}{TP + FN}$$

$$\text{False Positive Rate} = \frac{TP}{FP + TN}$$

Figure 39: Definitions of metrics.

Orbit	Map Type	Alpha	TP	FP	FN	TN
116	bmap	5%	291	102	84	273
		2.5%	255	78	120	297
		1%	228	51	147	324
	smap	5%	264	53	111	322
		2.5%	232	48	143	327
		1%	202	35	173	340
21	bmap	5%	311	117	64	258
		2.5%	296	86	79	289
		1%	264	65	111	310
	smap	5%	278	60	97	315
		2.5%	273	51	102	324
		1%	247	36	128	339

Table 11: Number of buildings with changes (TP, FP, FN, TN) for Orbit 116 and 21, with bmap and smap at different significance levels (alpha).

## Appendix B. Figures

---

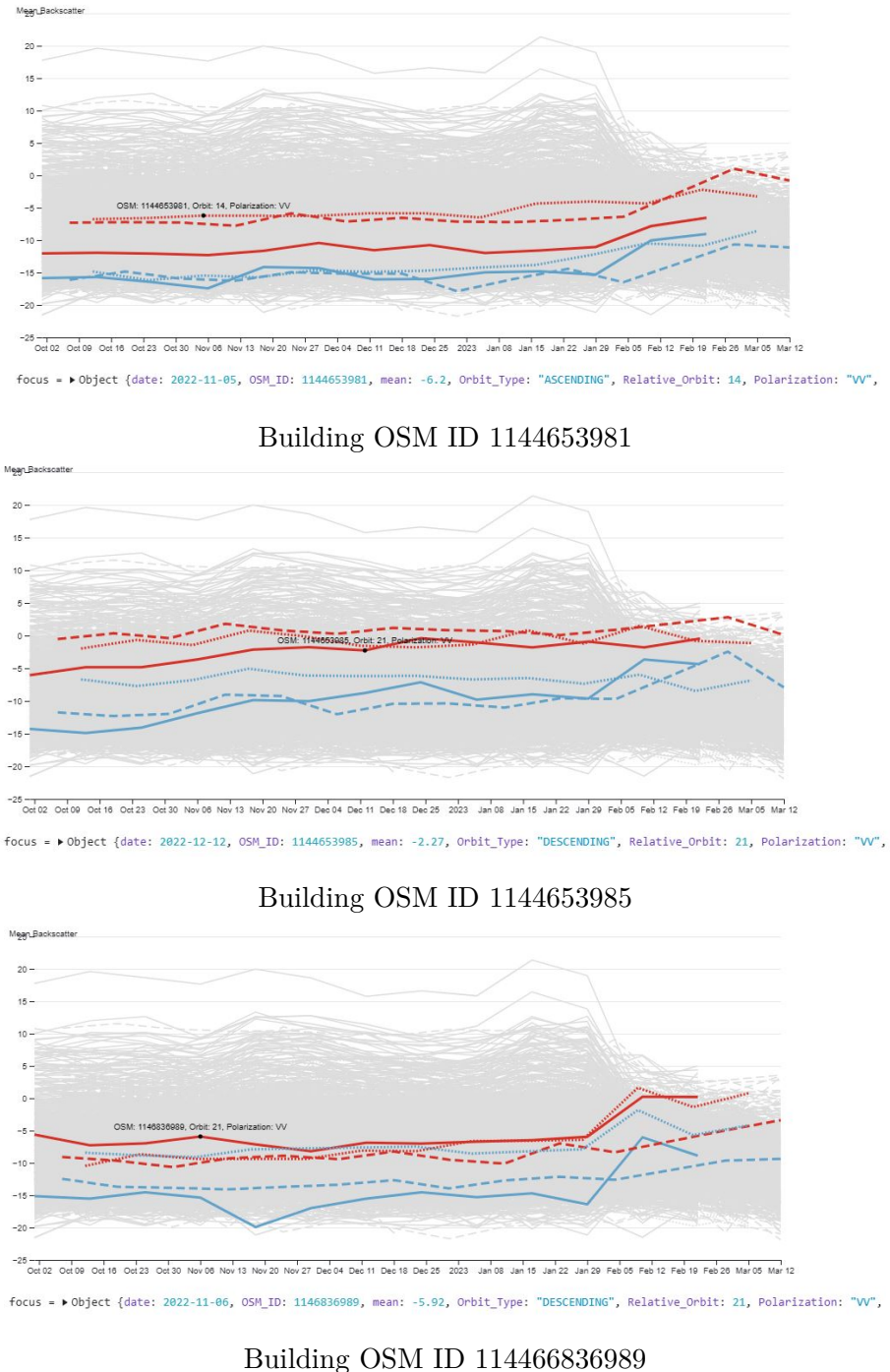


Figure 40: Temporal signatures of buildings in industrial zone with increasing trend.